

Louisiana Tech University

Louisiana Tech Digital Commons

Doctoral Dissertations

Graduate School

Spring 5-2022

Mitigation of End Zone Cracking in Precast Prestress Concrete Girders

Oluwatobi F. Babarinde

Follow this and additional works at: <https://digitalcommons.latech.edu/dissertations>

**MITIGATION OF END ZONE CRACKING IN PRECAST
PRESTRESSED CONCRETE GIRDERS**

by

Oluwatobi F. Babarinde, B.Sc., M.S.

A Dissertation Presented in Partial Fulfillment
of the Requirements of the Degree
Doctor of Philosophy

COLLEGE OF ENGINEERING AND SCIENCE
LOUISIANA TECH UNIVERSITY

May 2022

LOUISIANA TECH UNIVERSITY

GRADUATE SCHOOL

April 1, 2022

Date of dissertation defense

We hereby recommend that the dissertation prepared by

Oluwatobi F. Babarinde, B.Sc., M.S.

entitled **Mitigation of End Zone Cracking in Precast Prestress Concrete Girders**

be accepted in partial fulfillment of the requirements for the degree of

Doctor of Philosophy in Engineering, Materials & Infrastructure Systems Conc.



Chuanbing Shawn Sun
Supervisor of Dissertation Research

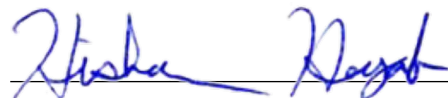


Jay Xingran Wang
Head of Engineering

Doctoral Committee Members:

Jay Xingran Wang
Shaurav Alam
Arun Jaganathan
Nazimuddin Wasiuddin

Approved:



Hisham Hegab
Dean of Engineering & Science

Approved:



Ramu Ramachandran
Dean of the Graduate School

ABSTRACT

Precast prestressed concrete girders have been widely used to construct bridges in the United States. Recent advancements in high-performance concrete and newly developed girder sections allow the span of girders to be extended significantly. Generally, bridges with longer spans require deeper girders and use more prestressing strands; the latter exacerbates the end zone cracking in pretensioned concrete girders when prestressing strands are released. Various types of end zone cracks have been observed, including horizontal and inclined cracks in the web, and bottom flange cracks.

This dissertation explores two possible options to mitigate the end zone cracking in precast prestressed concrete girders, including the use of shape memory alloys (SMAs) and ultra-high performance concrete (UHPC) at the girder ends. Experimental work was conducted on the use of SMA wires to apply vertical prestress in the end zone of prestressed girders to counter the bursting stresses as a result of prestress transfer. The end zone behavior of UHPC in prestressed girders was also studied to evaluate its effect on enhanced splitting resistance. The relationship between the splitting resistance from the vertical reinforcement and UHPC at the girder ends and applied prestressing force was examined experimentally and analytically.

The experimental study indicated that the use of SMAs successfully introduced vertical prestress at the prestressed concrete beam ends, and therefore can increase the splitting resistance and concrete cracking at prestress can be possibly mitigated or

eliminated. The laboratory tests showed that splitting resistance was significantly increased due to the use of UHPC at girder ends. It is suggested to keep the tensile stress limit of 20 ksi in the reinforcing bars to control the crack width, as specified for conventional concrete girders. The collected test data showed that the resulting splitting stresses in the prestressed UHPC girder ends were acceptable.

APPROVAL FOR SCHOLARLY DISSEMINATION

The author grants to the Prescott Memorial Library of Louisiana Tech University the right to reproduce, by appropriate methods, upon request, any or all portions of this Dissertation. It is understood that “proper request” consists of the agreement, on the part of the requesting party, that said reproduction is for his personal use and that subsequent reproduction will not occur without written approval of the author of this Dissertation. Further, any portions of the Dissertation used in books, papers, and other works must be appropriately referenced to this Dissertation.

Finally, the author of this Dissertation reserves the right to publish freely, in the literature, at any time, any or all portions of this Dissertation.

Author Barbara

Date April 5, 2022

DEDICATION

I dedicate this dissertation to Olayemi, my wife; and to Mayowa, our son.

TABLE OF CONTENTS

ABSTRACT.....	iii
APPROVAL FOR SCHOLARLY DISSEMINATION	v
DEDICATION.....	vi
LIST OF FIGURES	x
LIST OF TABLES.....	xiv
ACKNOWLEDGMENTS	xv
CHAPTER 1 INTRODUCTION.....	1
1.1 Research Objective	3
1.2 Research Organization.....	3
CHAPTER 2 LITERATURE REVIEW.....	4
2.1 End Zone.....	4
2.2 Shape Memory Alloy.....	6
2.3 Ultra-High Performance Concrete	8
2.4 Gergely-Sozen Method.....	10
2.5 Finite Element Method	10
CHAPTER 3 MITIGATION OF END ZONE CRACKS IN PRECAST PRESTRESSED CONCRETE GIRDERS USING SHAPE MEMORY ALLOYS.....	12
3.1 Tensile Strength Test of SMA Wires, Cables, and Strands	12
3.2 Prestrained SMA Wires, Strands, and Cables.....	15
3.3 Small-Scale Beam Tests	16
3.4 Full-Scale Beam Test – SMA	22

3.5	Finite Element Analysis.....	28
CHAPTER 4 END ZONE BEHAVIOR OF PRESTRESSED UHPC GIRDERS		31
4.1	UHPC Material Characterization Results	31
4.1.1	Concrete Cylinder Compression Test	32
4.1.2	Flexural Beam Test.....	33
4.2	Full-Scale Girder Tests using UHPC.....	34
4.2.1	Description of Specimens	35
4.2.2	Prestressing Strands	38
4.2.3	Strain Readings	41
4.3	Gergely-Sozen Analysis	46
4.4	Numerical Analyses	48
4.4.1	Material Models	49
4.4.2	Elements Technology and Meshing.....	52
4.4.3	Verifications.....	53
	Verification of FHWA Flexural Girder	53
	Verification of FHWA End Zone Girder	56
4.4.4	Girders A and B	59
	Sensitivity Studies.....	60
	Results.....	62
4.4.5	Analysis of a 9 ft-Deep Girder.....	65
CHAPTER 5 DISCUSSIONS		74
5.1	Girders Using SMAs.....	74
5.2	UHPC Girder End Zone.....	75
CHAPTER 6 CONCLUSIONS		79
APPENDIX A ANSYS COMMAND SNIPPET FOR NODE MERGE AND PRESTRESS SPECIFICATION		81

REFERENCES 84

LIST OF FIGURES

Figure 1-1: End zone cracks in a precast prestressed concrete beam (Okumus & Oliva, 2013)	2
Figure 2-1: Stresses in the end zone of a girder.(Hamilton et al., 2020)	5
Figure 2-2: Phase transformation and change in SMAs' crystalline structure (Alam et al., 2007)	6
Figure 2-3: A free-body diagram corresponding to the Gergely-Sozen equivalent beam method.	10
Figure 3-1: Stress-strain diagram of SMA wire.....	14
Figure 3-2: Stress-strain diagram of SMA strand.....	14
Figure 3-3: Testing of a SMA cable.	15
Figure 3-4: Stress-strain diagrams of SMA wires due to loading and unloading.....	16
Figure 3-5: Stress-strain diagrams of SMA strands due to loading and unloading.	16
Figure 3-6: Test setup of Beam No. 1.....	18
Figure 3-7: Test results of Beam No. 1.....	18
Figure 3-8: Test setup of Beam No. 2.....	19
Figure 3-9: Test results of Beam No. 2.....	20
Figure 3-10: Test setup of Beam No. 3.....	21
Figure 3-11: Test results of Beam No. 3.....	21
Figure 3-12: Test setup of Beam No. 4.....	22
Figure 3-13: Test results of Beam No. 4.....	22
Figure 3-14: Beam section and reinforcement detail.....	24
Figure 3-15: Reinforcement layout.....	24

Figure 3-16: Layout of the SMA cables.	25
Figure 3-17: Numbering of the steel strands.	26
Figure 3-18: Gauge readings due to heating Cable 1.....	27
Figure 3-19: Gauge readings due to heating Cables 2 to 4.....	28
Figure 3-20: Gauge readings due to tensioning steel strands.	28
Figure 3-21: FEA model of the full-scale beam.	29
Figure 3-22: Strain contour after activating all cables.....	30
Figure 4-1: UHPC compression test setup.....	32
Figure 4-2: UHPC cylinder sample after testing.	33
Figure 4-3: Flexural test setup of a UHPC beam.....	34
Figure 4-4: Prestressing bed during construction.	36
Figure 4-5: Geometry and layout of strands and reinforcement in Girder A.	36
Figure 4-6: Geometry and layout of strands and reinforcement in Girder B.....	37
Figure 4-7: Reinforcement details at girder ends. (a) Girder A end. (b) Ends between Girders A & B.	37
Figure 4-8: Strain gauge locations on web reinforcement. (a) Girder A. (b) Girder B. ..	38
Figure 4-9: Pretensioning bottom strands.....	39
Figure 4-10: Side view of Girders A & B.....	39
Figure 4-11: Post-tensioning of top flange steel strands.....	40
Figure 4-12: End of Girder A after all strands were prestressed.	40
Figure 4-13: Girder A rebar strain (microstrain) vs. time (second) plots at release of bottom strands.	41
Figure 4-14: Girder A rebar strain (microstrain) vs. time (second) plots after PT top strands.	42
Figure 4-15: Girder B rebar strain (microstrain) vs. time (second) plots at release of bottom strands.	42

Figure 4-16: Girder B rebar strain (microstrain) vs. time (second) plots after PT top strands.	43
Figure 4-17: Variation of rebar strains vs. locations. Error! Bookmark not defined.	
Figure 4-18: Variation of rebar forces vs. locations.	45
Figure 4-19: Resulting bursting forces at girder ends.....	46
Figure 4-20: Moment diagram at the end zone of Girder A and B due to pretension.	47
Figure 4-21: Moment diagram at the end zone of Girder A and B due to prestressing...	47
Figure 4-22: Typical stress-strain relationship for UHPC	50
Figure 4-23: Stress-strain relationship of steel strand.	52
Figure 4-24: Load-deflection comparison.	54
Figure 4-25: Longitudinal strain comparison.	54
Figure 4-26: Tensile stress-strain behavior of ANSYS DPC model.	55
Figure 4-27: ANSYS stress contour at 119 kip loading.	56
Figure 4-28: Details of girder tested by FHWA.	57
Figure 4-29: Bursting stress contour of FHWA girder.....	58
Figure 4-30: Comparison of stress in reinforcement bars.....	58
Figure 4-31: Comparison of stress in UHPC.....	59
Figure 4-32: Boundary conditions of ANSYS model.....	60
Figure 4-33: Effect of UHPC material model.....	61
Figure 4-34: Contour of bursting stresses using linear elastic model.....	62
Figure 4-35: Effect of element sizes on rebar stresses.....	62
Figure 4-36: Steel rebar stress contour for Girder A.	63
Figure 4-37: Steel rebar stress contour for Girder B.	63
Figure 4-38: Variation of rebar stress corresponding to locations in Girder A.	64
Figure 4-39: Variation of rebar stress corresponding to locations in Girder B.	64
Figure 4-40: Evolution of bursting strains at web-flange interface.	65

Figure 4-41: Cross-sectional details of a 9 ft deep girder.....	66
Figure 4-42: Stress in steel reinforcement bars of deep girder.	70
Figure 4-43: Force in steel reinforcement bars of deep girder.	71
Figure 4-44: UHPC stresses in deep girders.....	71
Figure 5-1: ANSYS bursting forces.....	78

LIST OF TABLES

Table 3-1: List of SMA wire, strand, and cable.....	13
Table 3-2: List of small-scale beams.	17
Table 4-1: Collected strain readings and calculated stresses and forces in the reinforcement.	44
Table 4-2: Summary of Gergely-Sozen analysis.	48
Table 4-3: Drucker-Prager concrete model constants.....	50
Table 4-4: HSD parameters.....	51
Table 4-5: Description of modeled deep girders.....	67
Table 4-6: Bursting forces in deep girders.....	68
Table 4-7: Summary of models studied to lower rebar stress.....	73

ACKNOWLEDGMENTS

I cannot begin to express my thanks to God who was, who is, and who will be forever. There will be no me without him, my creator, sustainer, and hope.

My topmost appreciation goes to my parents, Samuel and Elizabeth Babarinde, for the tremendous sacrifices that they made so that I can be where I am today. To my siblings, Tosin, Tolu, and Jesuloluwa, it has been a blessing to have grown up with you. Olayemi and Oluwamayowa, my wife and son, I love you both. Thank you for your ceaseless support.

This research work would not have been possible without Dr. Chuanbing Sun. His insight, hard work, and leadership have been inspiring. I appreciate the time and support from Dr. Jaganathan, Dr. Wang, Dr. Wasiuddin, Dr. Alam and last but not the least Dr. Weiss, who all served on my committee.

Especially, I would like to thank Nahid Farzana, Dinesha Kurupparachchi, Jared Headrick, Zihao Song, John Kraft, Devin, Reid, Chris Morgan, Dr. John Matthews, and other staff at TTC, for their assistance in the lab testing.

The author would like to thank the Louisiana Transportation Research Center and Precast/Prestressed Concrete Institute for funding the research projects.

CHAPTER 1

INTRODUCTION

Precast prestressed concrete girders have been widely used to construct bridges in the United States. Recent advancements in high-performance concrete and newly developed girder sections allow the span of girders to be extended significantly. Generally, bridges with longer spans require deeper girder cross sections and use more prestressing strands; the latter exacerbates the end zone cracking in pretensioned concrete girders when the prestressing strands are released. Various types of cracks can be observed in the end zone, including horizontal and inclined cracks in the web, and bottom flange cracks (**Figure 1-1**). Durability becomes a concern in girders with these cracks, especially when chloride or other deleterious ions penetrate the concrete reaching the steel reinforcement and causing corrosion.



Figure 1-1: End zone cracks in a precast prestressed concrete beam (Okumus & Oliva, 2013)

This dissertation presents two possible options to tackle the challenge of end zone cracking in precast prestressed concrete girders at time of prestress release. One approach involved the incorporation of shape memory alloys (SMAs) that allowed to introducing vertical prestressing forces in the end zone. The second approach was to use ultra-high performance concrete (UHPC) that contributed to the splitting resistance due to its post-cracking residual strength. Analytical and experimental studies were performed on both topics. This dissertation presents the full-scale testing results on a conventional prestressed concrete girder incorporating SMA wires, and two prestressed UHPC girders.

Chapter 2 covers the relevant background and literature review of both topics. Chapter 3 focuses on the experimental and analytical results of the tested girder involving the use of SMAs. Chapter 4 addresses the behavior of the UHPC girder end through laboratory testing and numerical analyses. Analytical methods include finite element

analysis (FEA) and Gergely-Sozen equivalent beam analysis, both of which were compared with the testing results.

Discussions of the results and analyses are included in Chapter 5 and concluding remarks are presented in Chapter 6.

1.1 Research Objective

The main objective of this dissertation was to evaluate the effect of advanced materials such as SMAs and UHPC on the end zone behavior of prestressed concrete girders. To accomplish this goal, the research work involved:

- (a) Testing the SMAs to determine their mechanical and transformation properties
- (b) Testing small-scale beams with SMAs
- (c) Testing a full-scale prestressed concrete girder with SMAs in the end zone
- (d) Analyzing test data and conducting numerical studies
- (e) Evaluating the effectiveness of UHPC in controlling end region cracking
- (f) Performing analyses of the tested UHPC girders

1.2 Research Organization

The findings of this research are presented in two key components:

1. Lab testing and analyses of a conventional girder using SMAs
2. Lab testing and analyses of two UHPC girders

CHAPTER 2

LITERATURE REVIEW

Numerous studies, including NCHRP Report 654 (Tadros et al., 2010), have been conducted on the evaluation and repair of end zone cracking. The current practice is to control the cracks to an acceptable extent by providing sufficient end zone reinforcement. In accordance with the current AASHTO LRFD Bridge Design Specifications (American Association of State Highway and Transportation Officials, 2020), vertical reinforcement shall be provided to resist four percent of the total prestressing force at prestress release and be located as close as possible to the girder end. When the girders include many prestressing strands, congested reinforcing details are mandatory to control the cracks. The end zone cracks, nevertheless, cannot be eliminated since the girders are only prestressed along their length, with no prestressing along the girder's height. As a result, the girder ends may crack due to the spalling and bursting forces at prestress release. This study investigated a novel way to provide vertical prestressing at the girder ends utilizing SMAs to alleviate the problem of end zone cracking. The effect of UHPC on the end zone behavior was also examined.

2.1 End Zone

End zone of a prestressed concrete girder refers to the portion over the length approximately equal to its depth. The location and magnitude of prestressing force, the transfer length, the quantity and arrangement of stirrups, presence of cracks, and the

beam cross section are the factors that influence the stress distribution in the end zone (Cousins et al., 2009). **Figure 5-1** shows the bursting, spalling, and splitting stresses that can cause to cracking in the end zone of a prestressed girder during prestress transfer.

Gergely-Sozen equivalent beam method (Gergely & Sozen, 1967), finite element analysis (FEA), and strut-and-tie model (Castrodale et al., 2002; Kannel et al., 1998; Lenschow & Sozen, 1965; Rogowsky & Marti, 1991; Tuan et al., 2004) are some of the numerous analytical methods that researchers have employed in the investigation of girder end zones. In addition to these analytical methods, experimental studies have been conducted on different pretensioned girders. The majority of the published research were conducted for normal-strength and high-strength concrete rather than UHPC.

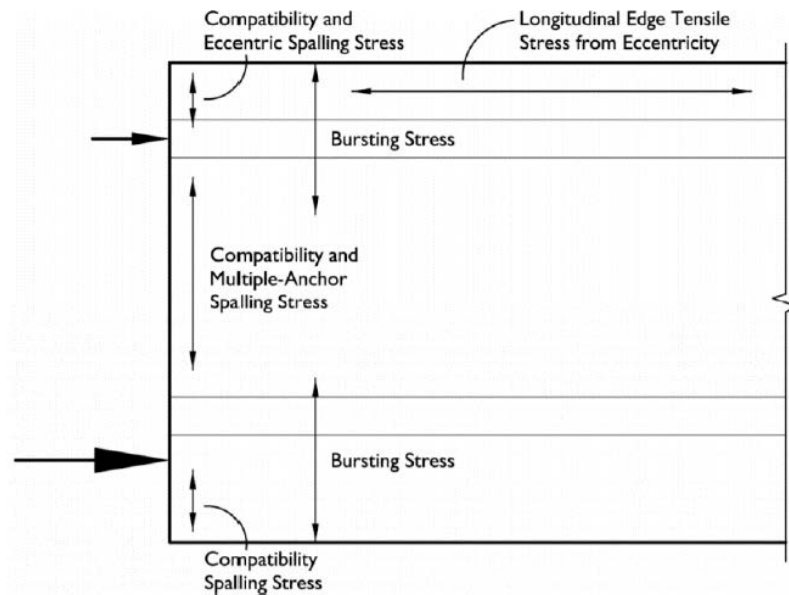


Figure 2-1: Stresses in the end zone of a girder.(Hamilton et al., 2020)

2.2 Shape Memory Alloy

SMAAs are characterized by a solid-solid, reversible phase transformation between two primary microstructural phases, martensite and austenite (Ozbulut & Hamilton, 2015). SMAAs' uniqueness rests in their ability to undergo large deformations and return to their undeformed shape by eliminating stress (superelasticity) or by heating (shape memory effect) (Alam et al., 2007). SMAAs exist in the martensite phase at relatively low temperatures and undergo a transformation to the austenite phase when heated. The following four distinct transformation temperatures characterize SMAAs (**Figure 2-2**): martensite start (M_s), martensite finish (M_f), austenite start (A_s), and austenite finish (A_f). SMA exists in a fully martensite state when its temperature is less than M_f and in a fully austenite state when its temperature is greater than A_f .

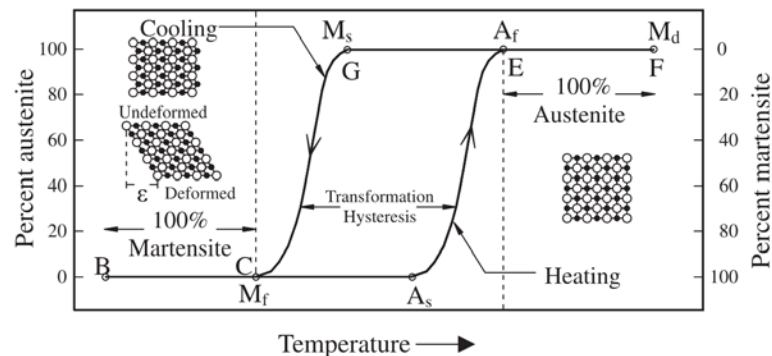


Figure 2-2: Phase transformation and change in SMAAs' crystalline structure (Alam et al., 2007)

The mechanical characteristics of SMAAs vary significantly depending on the respective quantities of the constitutive metals. Commonly used SMAAs in civil engineering structures include NiTi, NiTiNb, and iron-based SMAAs. Maji & Negret, (1998) were the first to use the shape memory effect in NiTi SMAAs to induce prestressing in concrete beams. SMA strands were pretensioned under the strain-hardening regime

and then embedded in model mortar beams. After the beams were cured, the SMA strands were activated with heat. El-Tawil & Ortega-Rosales (2004) tested small mortar beams that were prestressed using SMA tendons. Prestrained SMA tendons were placed in mortar beams and heated to result in the prestressing effect. Four-point loading beam tests showed that a significant level of prestressing force was attained in the beams. They studied both 2.5 mm-diameter NiTi and 6.3 mm-diameter NiTiNb wires. The NiTi wires exhibited appreciable constrained recovery stress, but all recovery stress was lost once the heat was removed. The NiTiNb wires appeared to be more suitable for permanent prestressing applications. Sherif et al. (2014) studied the use of SMAs to self-post-tension concrete beams by taking advantage of the grout's heat of hydration. They examined the temperature increase due to heat of hydration of four commercial grouts and explored the feasibility of activating NiTiNb alloys. A recovery stress of over 500 MPa was accomplished after cooling to ambient temperature. Moser et al. (2005) evaluated the feasibility of prestressing concrete beams using SMA short fibers. They shaped the SMA wires by inelastic elongation into loop- and star-shaped fibers. Mortar prisms were made by including multiple layers of SMA fibers. After the mortar hardened, the specimens were heated to activate the SMAs and the recovery stress introduced prestress to the specimens. As a result, the specimens were subject to compressive stresses up to 7 MPa.

Soroushian et al. (2001) conducted repair and strengthening of concrete members using iron-based SMAs. They found that the alloys could introduce post-tensioning forces to structural systems. SMA rods were adopted to transfer corrective forces to concrete beams for repair and strengthening. This concept was implemented to strengthen the bridge beams that had insufficient shear strength. Andrawes (2019) developed an Adaptive

Prestressing System (APS) for concrete crossties using SMAs. NiTiNb SMA wires were used to prestress concrete crossties at target regions. A variety of SMA prestressing system configurations were tested, including straight, L-shaped, and U-shaped wires. The test results confirmed that the SMA wires were capable of inducing prestressing forces at the specified locations of the crossties. Sinha et al. (2020) proposed a post-tensioning technique using unbonded near-surface mounted NiTiNb SMA wires. The wires with 2.5% prestrain resulted in a recovery stress of about 500 MPa after being Ohmic-heated in a restrained condition. They installed the SMA wires on pre-cracked concrete girders to assess the prestressing effect when the wires were heated. As a result, the crack widths were reduced by up to 74%.

A number of researchers have explored the feasibility of introducing prestressing to concrete beams using SMAs. The application of SMAs has been related to either new construction or repair/strengthening of concrete members. However, the use of SMAs at the end zone of prestressed concrete girders has not been evaluated yet. This study presents the first attempt to study its feasibility of increasing splitting resistance in prestressed concrete girders.

2.3 Ultra-High Performance Concrete

UHPC has attracted increasing interest because of its highly enhanced mechanical properties by comparison to conventional concrete. It has been implemented in different bridge components, including joints, piles, deck panels, and girders. Several federal and state agencies are funding research on the use of UHPC in bridge girders. A recently completed project sponsored by the PCI (Tadros et al., 2021) demonstrated the feasibility of a 250-ft long decked I-girder for bridges. The girders required a significant level of

prestress applied at the girder top flange to control camber, in order to avoid expensive and slow field operations of cast-in-place topping. As a result, this condition significantly increased the bursting stresses in the web. It is expected that the exceptional high tensile strength of UHPC would reduce the demand for bursting reinforcement at web ends due to prestress release. However, UHPC beams are featured with smaller sections and longer spans, which requires much higher prestress than the levels observed in the 1960s when the bursting reinforcement guidelines were developed (Marshall & Mattock, 1962).

The tensile strength of the UHPC varies and is based on the type, amount, and orientation of steel fibers spanning the crack, according to direct tensile strength tests. (Gowripalan & Gilbert, 2000). When a notched cylinder starts to crack, the average tensile stress typically starts to decrease at a crack width of about 0.2 mm and continues to decrease when the crack width increases (Behloul, 2000). Gowripalan & Gilbert (2000) recommended an average and maximum tensile stress of 0.73 ksi and 1.16 ksi, respectively, when a strut-and-tie model is adopted to design the end zone without using transverse reinforcement.

Hamilton et al. (2020) studied the approach of producing hybrid girders that included placement of UHPC at the girder ends and conventional self-consolidating concrete (SCC) mixture in the remainder of the girder to prevent end region cracking. They tested five 20-ft-long Florida-I 72 beam (FIB 72) and two 50-ft-long Florida-I 54 beam (FIB 54) UHPC-SCC hybrid girders. The lengths of the UHPC blocks at ends varied from 4 ft – 6 in. to 6 ft – 9 in. The contribution of bursting resistance from UHPC was determined based on a tensile strength of 800 psi. The experimental results demonstrated that UHPC ends exhibited maximum end region crack widths of 0.003 in.,

which were about 25% of the crack widths in the SCC ends. They confirmed that UHPC is a promising approach to reducing end region cracking.

2.4 Gergely-Sozen Method

The Gergely-Sozen equivalent beam method is based on equilibrium conditions of the cracked end zone. The resisting moment is provided by the tension force, T , in the end zone reinforcement, and the compression force in the concrete, C (Figure 2-3). It is believed that the Gergely-Sozen equivalent beam method can generate reasonable results (Tuan et al., 2004).

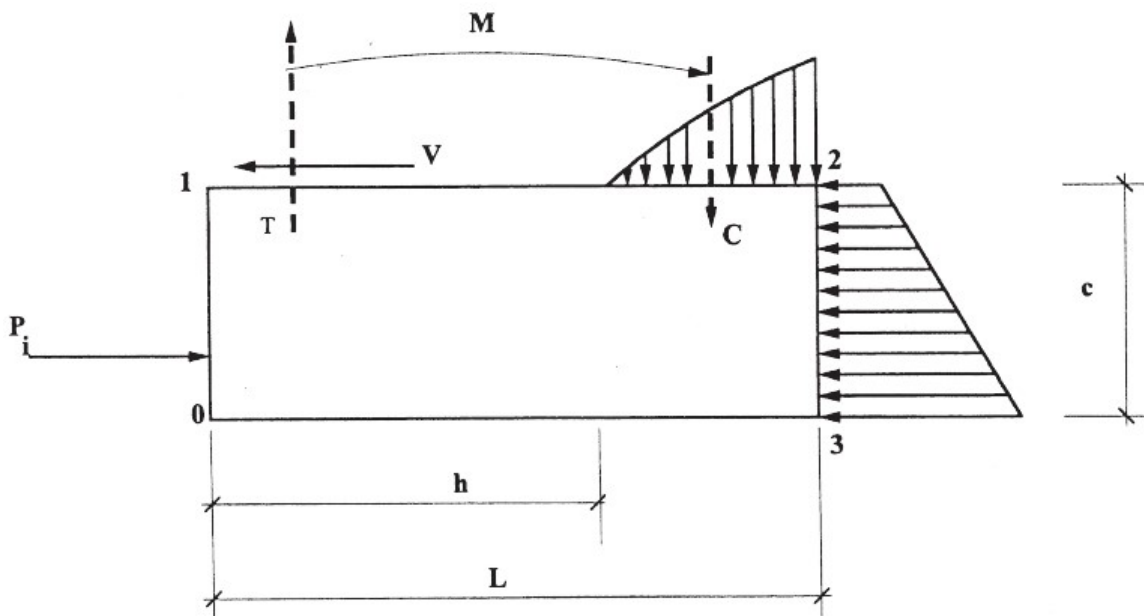


Figure 2-3: A free-body diagram corresponding to the Gergely-Sozen equivalent beam method.

2.5 Finite Element Method

FEA models that include the prestressing strands in the top and bottom flanges of girders can be used to investigate bursting stresses in girders with and without end zone reinforcement. Many researchers have employed the FEA approach for end zone analyses

and calibrated the FEA models by testing prestressed concrete girders. Ronanki et al. (2019) conducted experimental and analytical investigation of end zone cracking in BT-78 girders.

The strut-and-tie model is effective in investigating the stress flow in the end zone and locating zones of concrete tension. Davis et al. (2005) used this approach to analyze PCBT girders, calibrated the models using field observations, and recommended different working stress in the reinforcement to limit crack width within 0.023 in. after prestress release. Cousins et al. (2009) further refined the strut-and-tie based design approach, verified the models using a 65-ft-long PCBT-53 girder, and recommended anchorage zone details for the Virginia Department of Transportation. As a strength limit analysis method, however, the strut-and-tie model in calculating the amount of bursting reinforcement may be overly conservative.

CHAPTER 3

MITIGATION OF END ZONE CRACKS IN PRECAST PRESTRESSED CONCRETE GIRDERS USING SHAPE MEMORY ALLOYS

End zone cracking in prestressed concrete girders necessitates a set of tests in order to find a solution. This chapter discusses the tests performed on the SMA materials themselves, on small-scale beams consisting of SMA wire/cable and normal strength concrete, and finally a full-scale prestressed concrete beam with prestrained SMA components in the end zone. The mechanical properties of SMAs and their prospective usage in prestressed concrete girders were studied using material testing and small-scale beam tests.

3.1 Tensile Strength Test of SMA Wires, Cables, and Strands

Several suppliers were contacted to order NiTi and NiTiNb SMAs. Unfortunately, most of the suppliers can only provide small-diameter wires and no suitable NiTiNb SMAs were available. As a result, NiTi SMA wires, strands, and cables from one supplier were used in this project. **Table 3-1** lists the SMA wire, strand, and cable, their descriptions, cross sectional areas, and A_f .

Table 3-1: List of SMA wire, strand, and cable.

Item	Description	Area (mm ²)	A_f (°C)
Wire	2.0 mm diameter	3.2	94
Strand	7-wire strand; 2.8 mm diameter	4.8	65
Cable	7-strand cable; 8.4 mm diameter	33.5	65

An MTS machine was used to determine the stress-strain responses of SMA wires and strands up to failure. The clear length of the wire and strand between the grips was approximately 254 mm. When the wire or strand was loaded, a displacement-control option was used with a loading rate of 5.1 mm per minute. An initial force of 89 N was applied to eliminate the sag in the samples. The stress-strain diagrams of the wire and strand are plotted in **Figure 3-1** and **Figure 3-2**, respectively. The wires reached an ultimate strength of approximately 1,069 MPa with a corresponding strain of about 13%. The ultimate strength of the strand was about 1,200 MPa with an ultimate strain of approximately 11%. Because the grips in the MTS machine cannot accommodate the SMA cable, its tensile strength was estimated using a hydraulic mono-strand jack. Ultra-high strength concrete (UHPC) blocks were placed side by side and the cable was pulled through the slots in the blocks. One end of the cable was anchored by a chuck, while the other end was tensioned by the jack (**Figure 3-3**). Two cables were tested to failure when the loads reached approximately 38.3 kN.

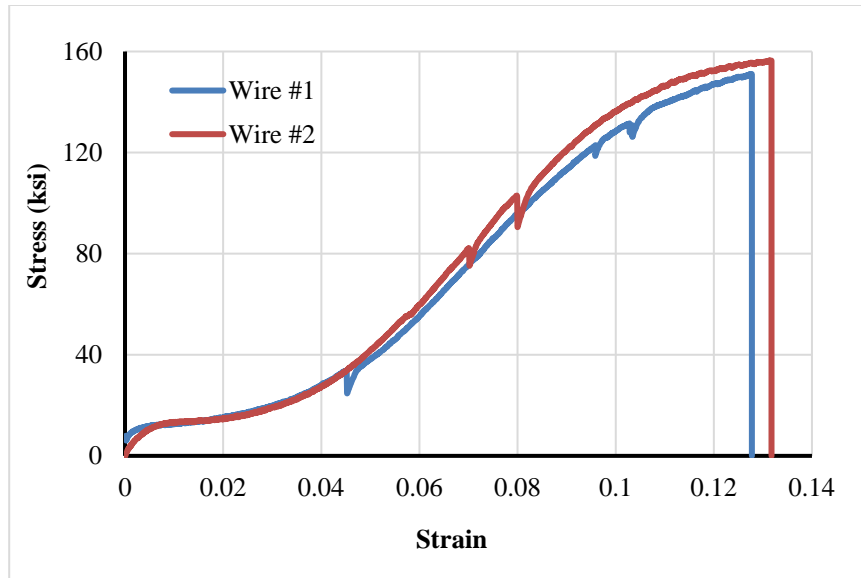


Figure 3-1: Stress-strain diagram of SMA wire.

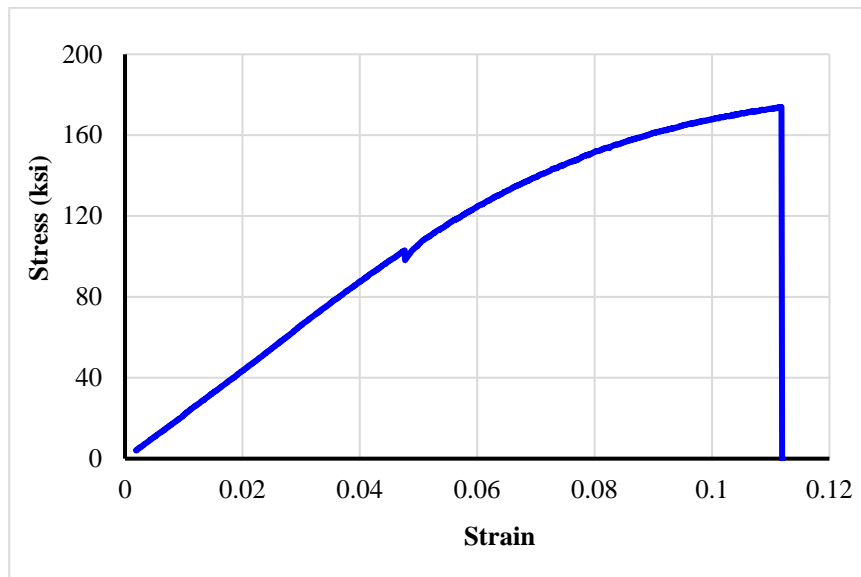


Figure 3-2: Stress-strain diagram of SMA strand.



Figure 3-3: Testing of a SMA cable.

3.2 Prestrained SMA Wires, Strands, and Cables

At room temperature, the wires and strands were loaded and then unloaded using the MTS machine to introduce residual strains. The maximum stresses introduced in the wires and strands were slightly lower than their ultimate tensile strengths to maximize the residual strains. During the unloading process, a force-control option was used with a rate of 22.2 N per second. As a result, approximately 8% and 2% residual strains were introduced in the wires and strands, respectively. **Figure 3-4** and **Figure 3-5** plot the stress-strain diagrams of the wires and strands subject to loading and then unloading. Five wires and five strands were tested, and comparable plots were achieved among each type of samples. Similarly, the SMA cables were tensioned to 34.7 kN using the mono-strand jack and then released to result in residual strains. As a result, the residual strains in the cables reached approximately 1.7%.

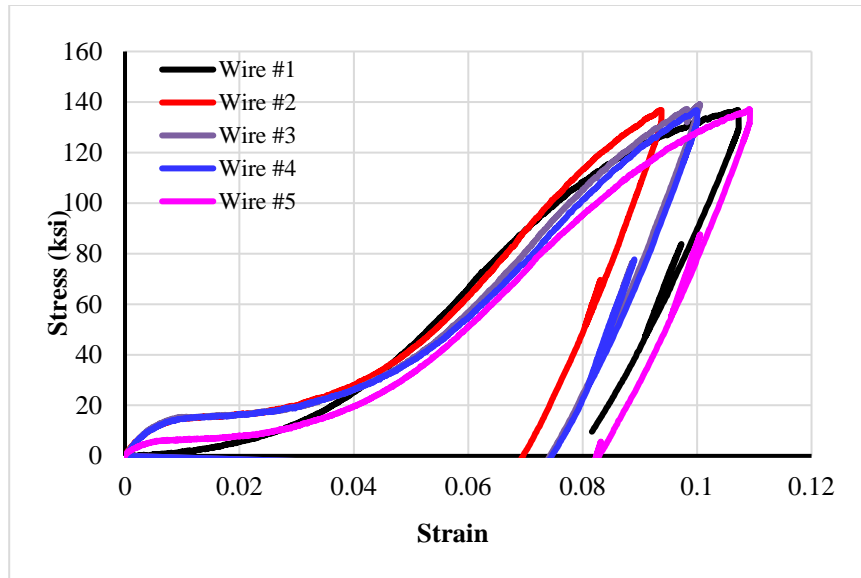


Figure 3-4: Stress-strain diagrams of SMA wires due to loading and unloading

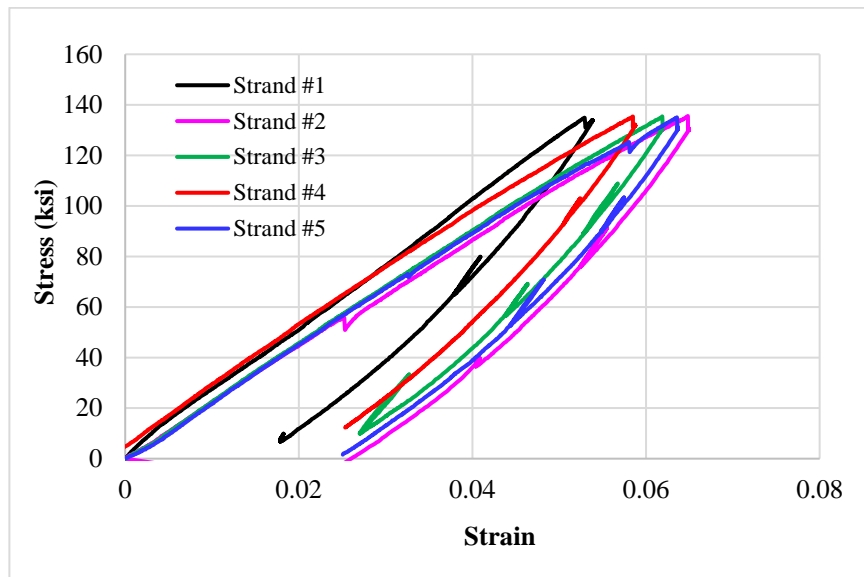


Figure 3-5: Stress-strain diagrams of SMA strands due to loading and unloading.

3.3 Small-Scale Beam Tests

Prestrained NiTi wires, strands, and cables were inserted in small-scale beams built of Type-M mortar or concrete to evaluate the feasibility of introducing prestressing in concrete beams. With the mortar or concrete, the SMA reinforcement was either

bonded or unbonded. The beams, SMA kinds, use of mortar or concrete, beam cross section measurements, beam lengths, and bonded or unbonded SMA types are all summarized in **Table 3-2**. Strength of the mortar was determined by testing 51 mm-cube specimens. The following section describe various types of specimens and their test results.

Table 3-2: List of small-scale beams.

Beam No.	SMA type	Mortar or concrete	Beam section (mm x mm)	Beam length (mm)	Bonded or unbonded
1	Two wires	Mortar	25 x 25	305	Bonded
2	One strand	Mortar	25 x 25	305	Bonded
3	One cable	Concrete	51 x 51	305	Unbonded
4	One cable	Concrete	51 x 51	305	Bonded

The test setup of Beam No. 1 is shown in **Figure 3-6** in which two SMA wires were bundled and bonded with the mortar. A pair of strain gauges were provided at opposite faces of the beam to measure the axial strain experienced. **Figure 3-7** plots the average readings from these two strain gauges versus time. At about 800 seconds, there was a considerable decline in the strain values which was caused by the recovery stress of the wire after being electrically heated. The beam had a maximum compressive strain of approximately 250 microstrain. The strains gradually increased afterward, partially because the concrete was heated up and expanded. When the concrete temperatures dropped slowly, the beam regained some compressive strains. When the concrete

temperature stabilized at the end, the compressive strain was approximately 160 microstrain.



Figure 3-6: Test setup of Beam No. 1.

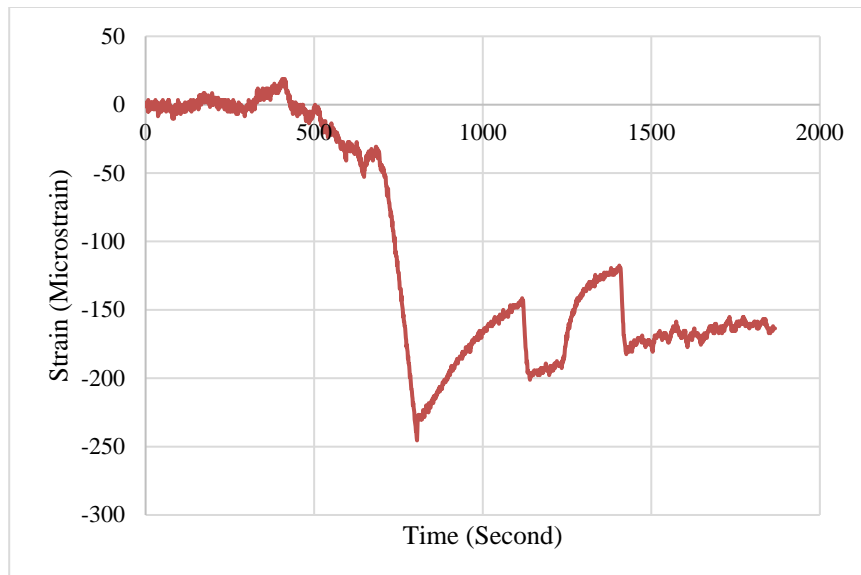


Figure 3-7: Test results of Beam No. 1.

Figure 3-8 shows the test setup of Beam No. 2, in which one SMA strand was bonded with the mortar. A pair of strain gauges were provided at opposite faces of the beam to measure the axial strain experienced. The average readings from the two gauges versus time were plotted in **Figure 3-9** after electrically heating the strand. The beam exhibited a maximum compressive strain of approximately 140 microstrain when the strand was activated. When the concrete returned to room temperature, the compressive strain was approximately 40 microstrain, i.e., a significant portion of the recovery stress was lost.

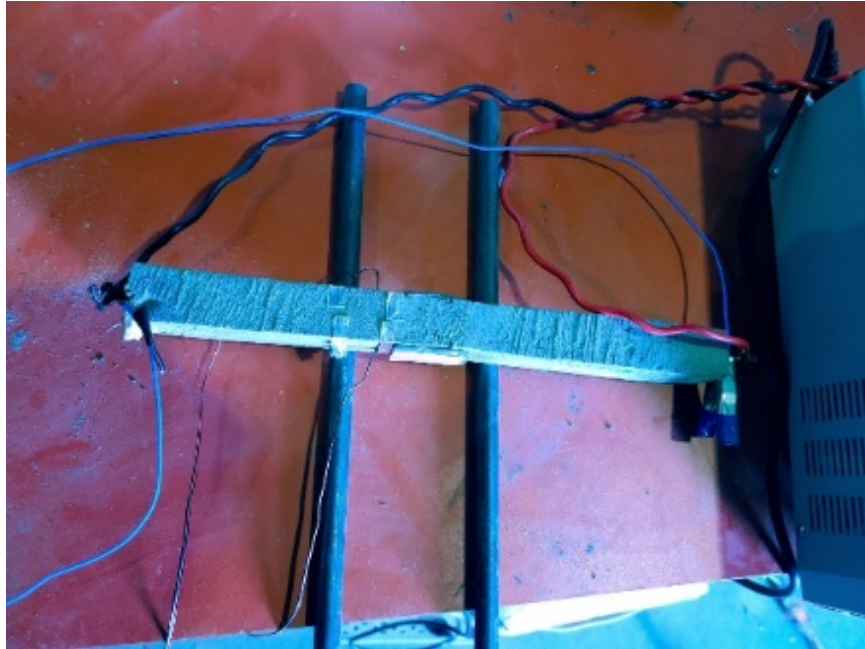


Figure 3-8: Test setup of Beam No. 2.

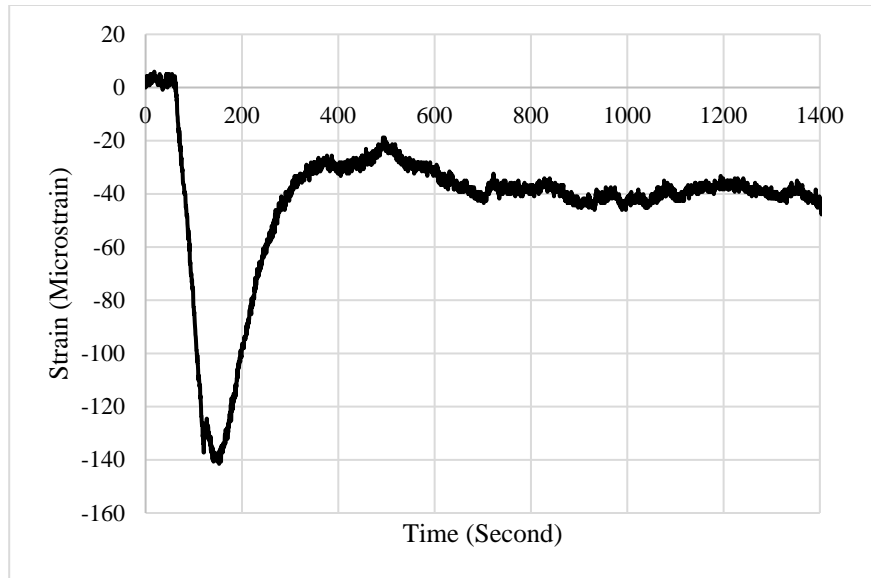


Figure 3-9: Test results of Beam No. 2.

Figure 3-10 shows the test setup of Beam No. 3, in which one SMA cable was housed in a PVC pipe and unbonded with the concrete. The cable was anchored by a chuck at each beam end. One anchor was fully seated when the cable was prestrained. When the other anchor was installed to the beam, the cable was re-tensioned to approximately 3.4 kN to remove the anchor set loss. One strain gauge was placed at each side face of the beam. **Figure 3-11** plots the average readings from the two gauges versus time. When the cable was electrically heated, the beam was subject to a maximum compressive strain of 50 microstrain, which corresponded to about 1.2 MPa compressive stress in the concrete beam. This indicated that the recovery stress resulted in a compressive force of approximately 3.1 kN. However, when the heating was removed, the recovery stress was gradually lost.



Figure 3-10: Test setup of Beam No. 3.

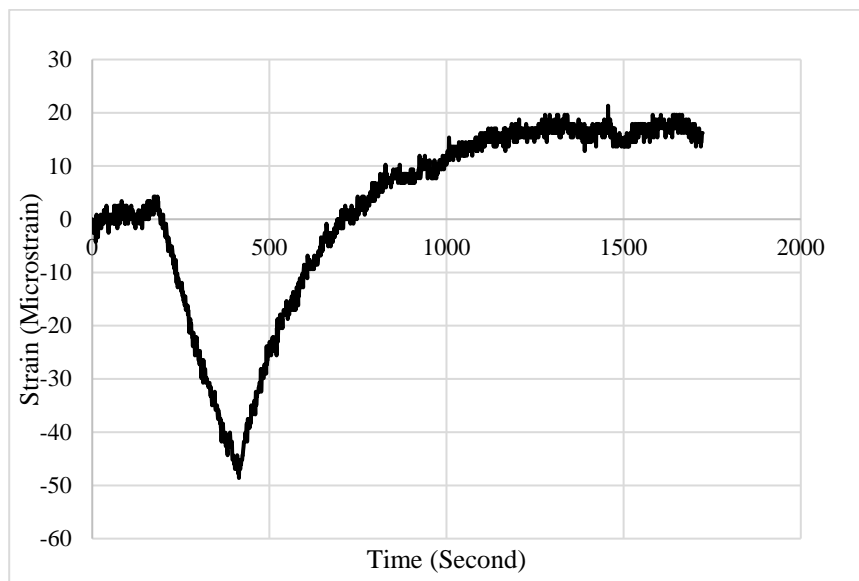


Figure 3-11: Test results of Beam No. 3.

Figure 3-12 shows the test setup of Beam No. 4, in which one SMA cable was bonded with the concrete. One strain gauge was installed at each side face of the beam. **Figure 3-13** plots the average readings from the two gauges versus time. When the cable was activated, the beam was subject to a maximum compressive strain of 10 microstrain, which corresponded to about 0.24 MPa compressive stress in the concrete beam. It

indicated that the recovery stress caused a compressive force of approximately 0.6 kN. The recovery stress was relatively small primarily because of the short beam length, which was insufficient to develop the cable. Similarly to **Figure 3-11**, the recovery stress was gradually lost when the heating was removed.



Figure 3-12: Test setup of Beam No. 4.

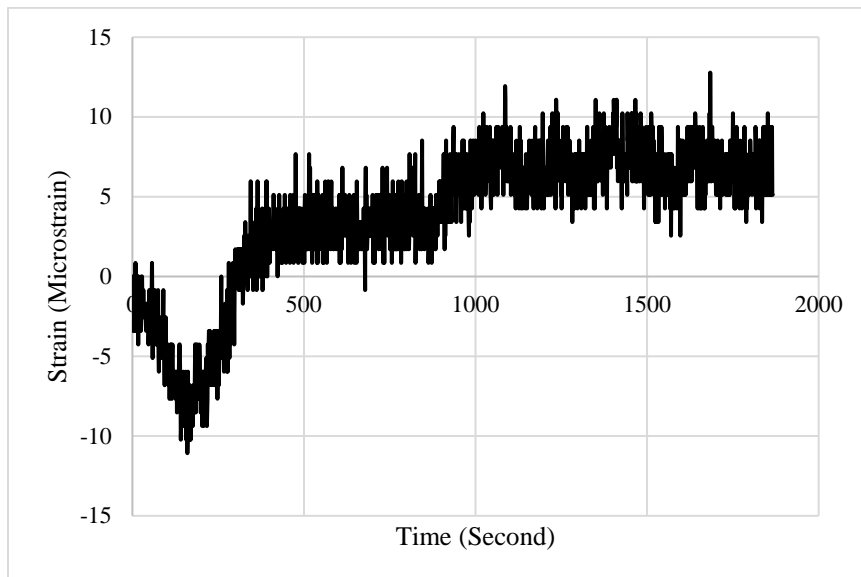


Figure 3-13: Test results of Beam No. 4.

3.4 Full-Scale Beam Test – SMA

A concrete beam was made in the lab to study the feasibility of using SMAs in eliminating end zone cracks at prestress release. As shown in **Figure 3-14**, the beam

cross section is comparable to an AASHTO Type I beam and its flanges were simplified for ease of forming. The beam was 610 mm deep, and its web was 152 mm wide. The beam flanges were 305 mm wide and 203 mm thick. The reinforcement included #13 stirrups in both flanges, pairs of #13 C-bars in the web, and #13 longitudinal bars. The C-bars were spaced at approximately 610 mm along the beam length except at the ends, in which two pairs were placed at 254 mm and 406 mm from each beam end, respectively. The shear reinforcement was intentionally provided far from the beam end to eliminate its contribution to the splitting resistance. The stirrups in the flanges were spaced at 102 mm for 610 mm from each beam end to provide sufficient confinement for the prestressing strands. Four 15.2 mm-diameter, Grade 1862 strands were placed in flexible polymer plastic tubing in each flange. **Figure 3-15** shows the layout of the prestressing strands and reinforcing bars. One of the beam's ends includes three pairs of ½ in.-diameter PVC pipes installed vertically to house the SMA cables, and six SMA wires in the beam web.

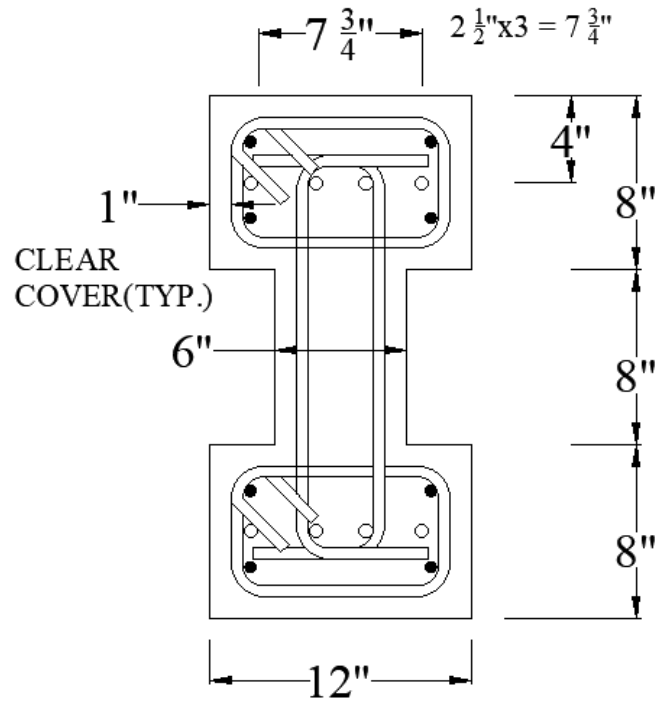


Figure 3-14: Beam section and reinforcement detail.



Figure 3-15: Reinforcement layout.

The beam formwork was removed three days after the concrete pour when the compressive strength reached about 23 MPa based on cylinder tests. Four SMA cables were subsequently installed at one beam end and the cable ends were anchored by chucks. The first cable was electrically heated prior to installation of the other three cables. The heating was stopped after the cable's temperature reached approximately 100 °C and the current was about 39 amps. Afterward, the other three cables were placed. Their distances measured to the beam end varied from 89 to 229 mm to allow evaluation of their effect on the splitting resistance (**Figure 3-16**).

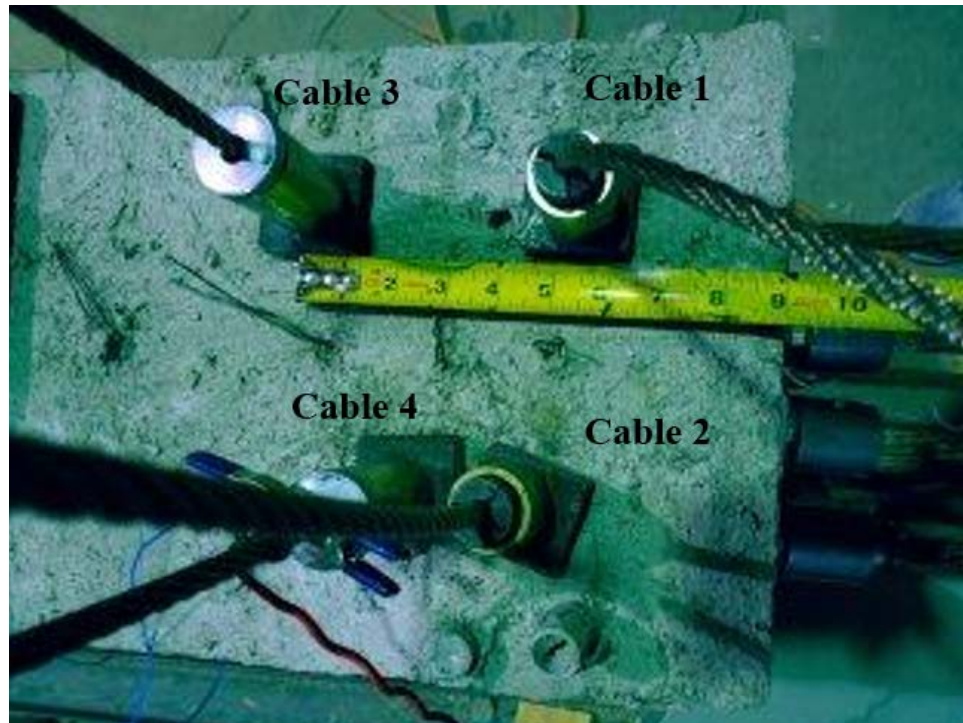


Figure 3-16: Layout of the SMA cables.

The longitudinal steel strands were post-tensioned four days after the concrete pour. The strands were numbered and tensioned in an order to maintain symmetrical loading (**Figure 3-17**). Two strain gauges were installed at the end face of the beam web.

All steel strands were tensioned at one beam end following the sequence from strand No. 1 to 8 as marked in **Figure 3-17**. As an average, each strand was jacked to approximately 60.7 kN. The strands were not fully tensioned to the maximum allowable force due to the relatively low concrete strength at the time of testing.



Figure 3-17: Numbering of the steel strands.

The readings of the two strain gauges at the beam end were collected and plotted in **Figure 3-18** to **Figure 3-22**. **Figure 3-18** shows the gauge readings when Cable 1 was electrically heated. The recovery stress of the SMA cable resulted in strain changes of approximately 15 microstrain at one gauge and 10 microstrain at the other gauge. As an

average, these strains corresponded to approximately 0.3 MPa compressive stress in the web. Similarly, **Figure 3-19** illustrates the gauge readings when Cables 2 to 4 were electrically heated. Activating Cable 2 resulted in approximately 15 microstrain at both gauges. Because Cables 3 and 4 were located further from the beam end as compared to Cables 1 and 2, their effect was not so significant and caused approximately 10 microstrain. As a total, the four cables introduced about 40 microstrain or 1.0 MPa compressive stress at mid-height of the beam end. On the other hand, the recovery stress of the SMA wires was insignificant and therefore was not reported. After all steel strands were tensioned, the gauge readings corresponded to an average strain change of approximately 80 microstrain (**Figure 3-22**), or 1.9 MPa tensile stress at the instrumented locations. Because the modulus of rupture for concrete was about 3.0 MPa, the resulting tensile stress was not high enough to crack the concrete. Therefore, no cracking was observed in the web.

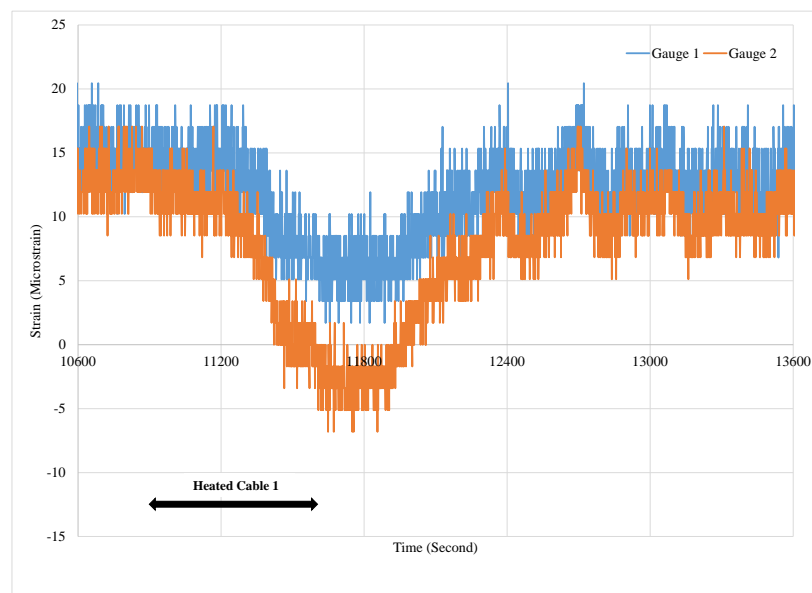


Figure 3-18: Gauge readings due to heating Cable 1.

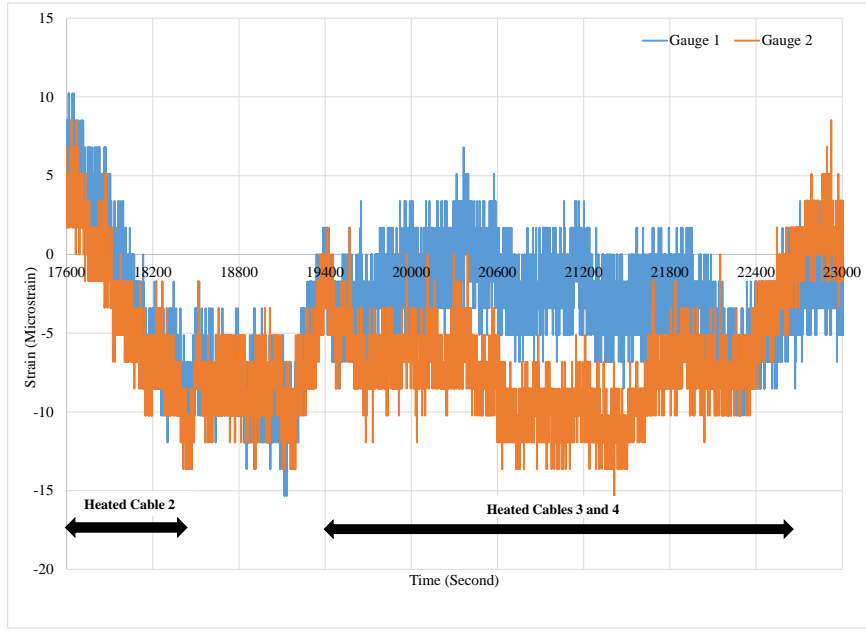


Figure 3-19: Gauge readings due to heating Cables 2 to 4.

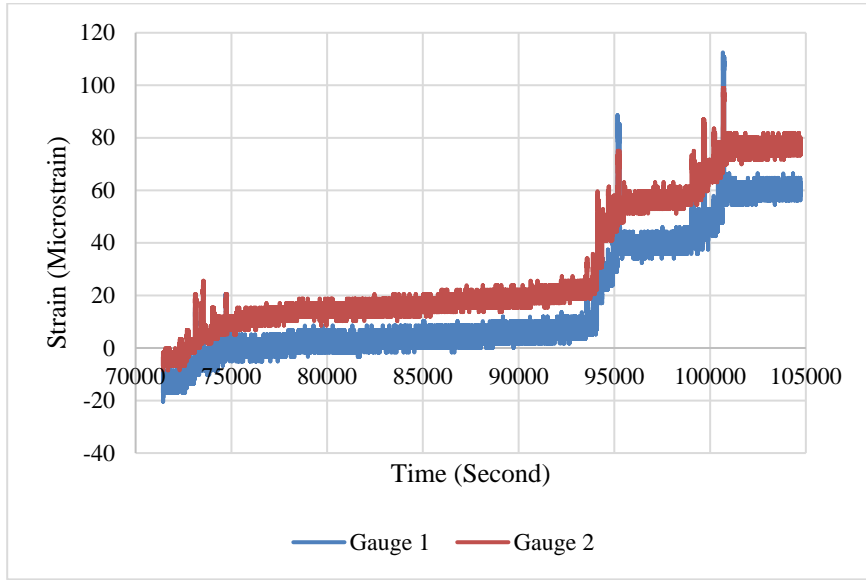


Figure 3-20: Gauge readings due to tensioning steel strands.

3.5 Finite Element Analysis

Finite element analysis (FEA) was conducted to simulate the behavior of the beam ends using ANSYS R19.2. The FEA model was developed to capture the end zone response

when the SMA cables were activated, and prestressing strands were released. **Figure 3-21** shows the FEA model, in which half of the beam length was accounted for. The analysis showed a strain of approximately 10 microstrain at one strain gauge, which is comparable to the collected gauge reading. Similarly, **Figure 3-22** plots the strain contour after all cables were activated. The FEA model also accounted for the longitudinal prestressing force due to the steel strands. The analysis results were slightly higher than the strain gauge readings. It confirmed that the corresponding stresses in the web were less than the modulus of rupture for concrete.

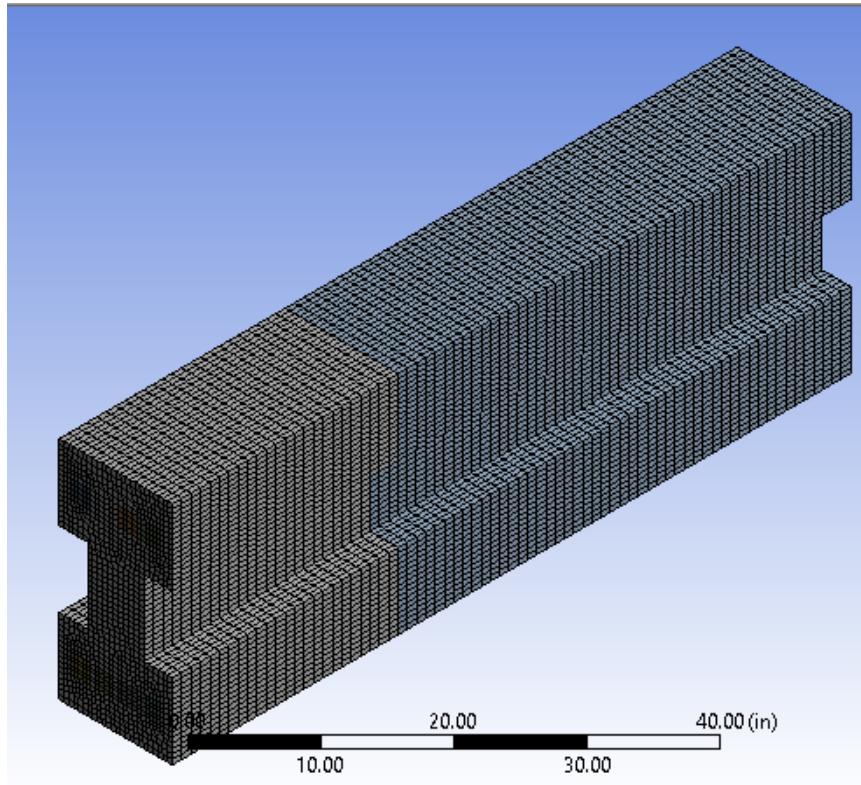


Figure 3-21: FEA model of the full-scale beam.

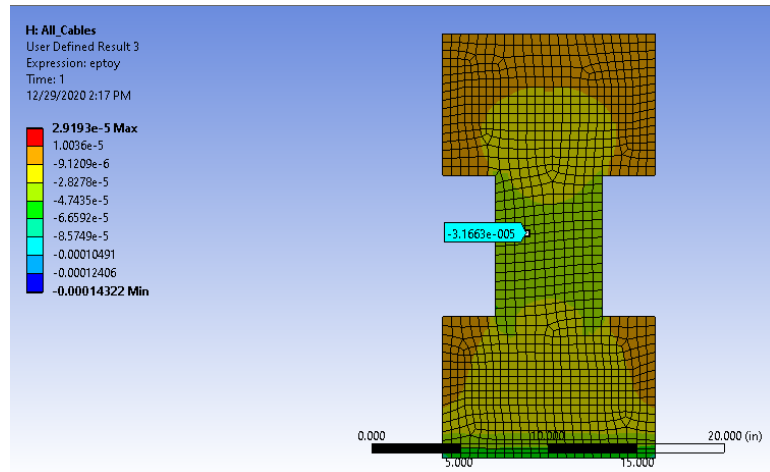


Figure 3-22: Strain contour after activating all cables.

CHAPTER 4

END ZONE BEHAVIOR OF PRESTRESSED UHPC GIRDERS

The end zone behavior of UHPC girders was studied and the experimental tests and findings were presented. The lab testing results were used to validate and calibrate the numerical analyses. This section describes the preparation of specimens, instrumentation, and test results. Furthermore, the Gergely-Sozen and Finite Element analyses complementing the tested girders are also presented.

4.1 UHPC Material Characterization Results

The UHPC material used in this research was the Ductual® Infrastructure 130 supplied by Lafargeholcim. This is a proprietary mix-design consisting of the following:

1. Premix
2. Water (with ice substitution depending on temperature)
3. Ductal F4 admixture
4. Steel fibers (2%)

These materials were mixed in an Imer 750 Mortarman Mixer following the UHPC supplier's instructions. Material characterization tests, such as cylinder compressive strength and flexural beam tests, were used to determine the fundamental characteristics of this UHPC.

4.1.1 Concrete Cylinder Compression Test

The compressive strength of concrete is its primary properties and other properties correlate to it. UHPC cylinder samples were prepared and cured and tested at different ages to capture the evolution of the compressive strength and to indicate the early-age strength at prestress release. ASTM Designation: A 370 procedures was followed for UHPC and conventional concrete, respectively.

The samples as shown in **Figure 4-1** were fitted with caps and tested with vertical servo-controlled hydraulic rams attached to the data acquisition software. In comparison with conventional concrete, the UHPC samples, as shown in **Figure 4-2**, do not become powdered as a result of complete crushing due to the steel fibers that still holding the matrix together. The cylinder compressive tests showed 10.0 ksi strength at 24 hours and 14.0 ksi at 3 days when cured in lab conditions.



Figure 4-1: UHPC compression test setup.



Figure 4-2: UHPC cylinder sample after testing.

4.1.2 Flexural Beam Test

The modulus of rupture is a property of concrete that indicates its tensile strength. The tensile strength of UHPC is of interest because it can be significant, unlike the tensile strength of conventional concrete, which is typically negligible. Hence, the UHPC material contributes substantially to bursting resistance in the end zone of prestressed girders. 4 in. x 4 in. x 14 in. UHPC samples were tested according to ASTM C1609/C1609M. UHPC beam samples were set up as shown in **Figure 4-3** to apply third-point loading and capture the vertical displacement at the midspan. This configuration introduces a uniform moment in the middle-third portion of the beam. Loading rates applied by the servo-controlled hydraulic ram are depended on the magnitude of the measured deflection. Up to $L/900$ deflection a rate of 0.002 in./min was used, and beyond

this point we used 0.004 in./min. The attached LVDT was used to measure the vertical deflection of the beam samples during the test.

The first-peak and residual strengths define the flexural behavior of UHPC. First-peak strengths, measured at the onset of cracking strengths, for the 28-days old samples, were 1.84 ksi and 1.31 ksi with an average strength of 1.58 ksi. The peak flexural tensile stress exceeded 3.1 ksi.



Figure 4-3: Flexural test setup of a UHPC beam.

4.2 Full-Scale Girder Tests using UHPC

An experimental investigation was performed to evaluate the end zone behavior of UHPC girders at prestress release. The lab testing results were used to validate and calibrate the numerical analyses. This section describes the preparation of specimens, instrumentation, and test results.

4.2.1 Description of Specimens

Two UHPC I-girders (Girders A and B) were made on a 15-ft-long prestressing bed, which can accommodate a total of 27 pretensioning strands at bottom. **Figure 4-4** shows the prestressing bed during construction, which included two concrete edge beams, 24 in. wide x 42 in. deep, and steel assemblies for pretensioning strand anchorages. The two girders had identical dimensions and were 2 ft-8 in. deep and 6 ft in length. Each girder weighed approximately 2,682 lbs. The girders used 0.6 in.-diameter, Grade 270 strands and Grade 60 reinforcing bars. Girder A included 27 bottom strands and 13 top strands (**Figure 4-5**). Girder B had 21 bottom strands and 9 top strands, respectively (**Figure 4-6**). The bottom strands were pretensioned and unbonded top strands were post-tensioned using a monostrand jack. PVC pipes were installed to accommodate the top strands in both girders and a few bottom strands in Girder B. No. 4 reinforcing bars were placed in the girder top and bottom flanges in both girders. Girders A and B included No. 5 and No. 4 web reinforcement at the girder ends, respectively (**Figure 4-7**). The end zone reinforcement, including the web reinforcement, and top and bottom flange reinforcement, was spaced at 2 in. in both girders. Four pairs of web reinforcement were placed within a distance equal to one-fourth girder height at each girder end. All reinforcement maintained a minimum of 1 in. concrete clear cover. Both girders included No. 4 projected bars for lifting. Strain gauges were installed at mid-heights of the vertical reinforcing bars near girder ends to capture the stress flow after strands were prestressed. It is understood based on previous research that the strains vary along the rebar height and the peak value typically occurs near the section centroid. Because the section centroid of the tested girder is close to its mid-height, the strain gauges were installed at

mid-height of web reinforcement. The numbering of the strain gauges in both girders is illustrated in **Figure 4-8**. At least one strain gauge was installed at each pair of web reinforcement.



Figure 4-4: Prestressing bed during construction.

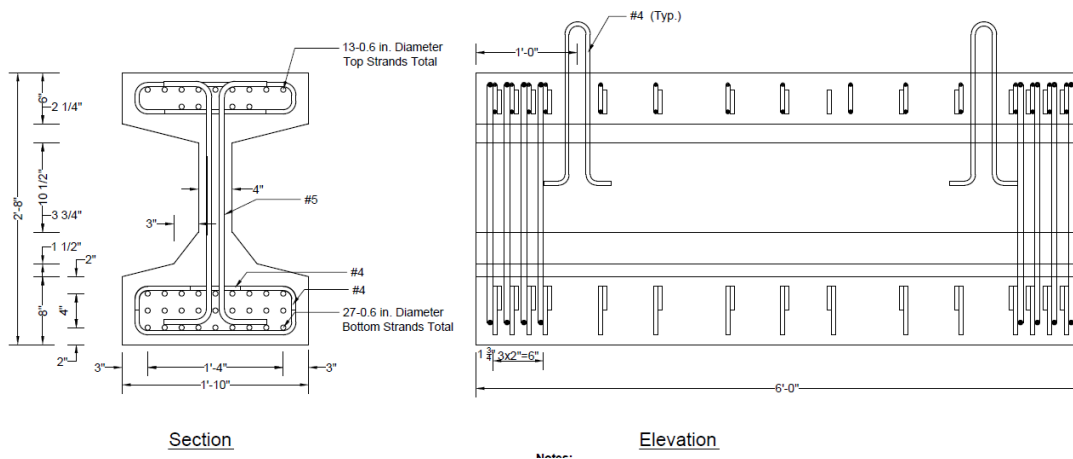


Figure 4-5: Geometry and layout of strands and reinforcement in Girder A.

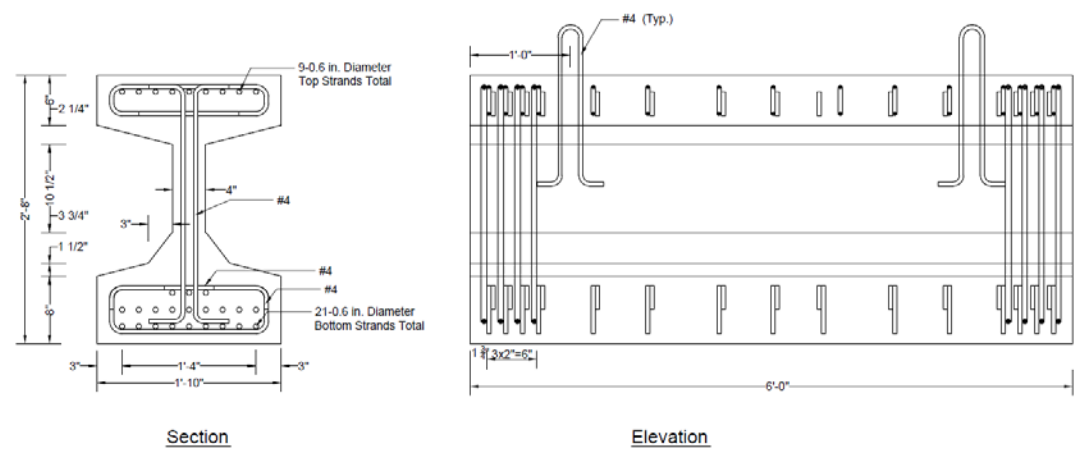


Figure 4-6: Geometry and layout of strands and reinforcement in Girder B.

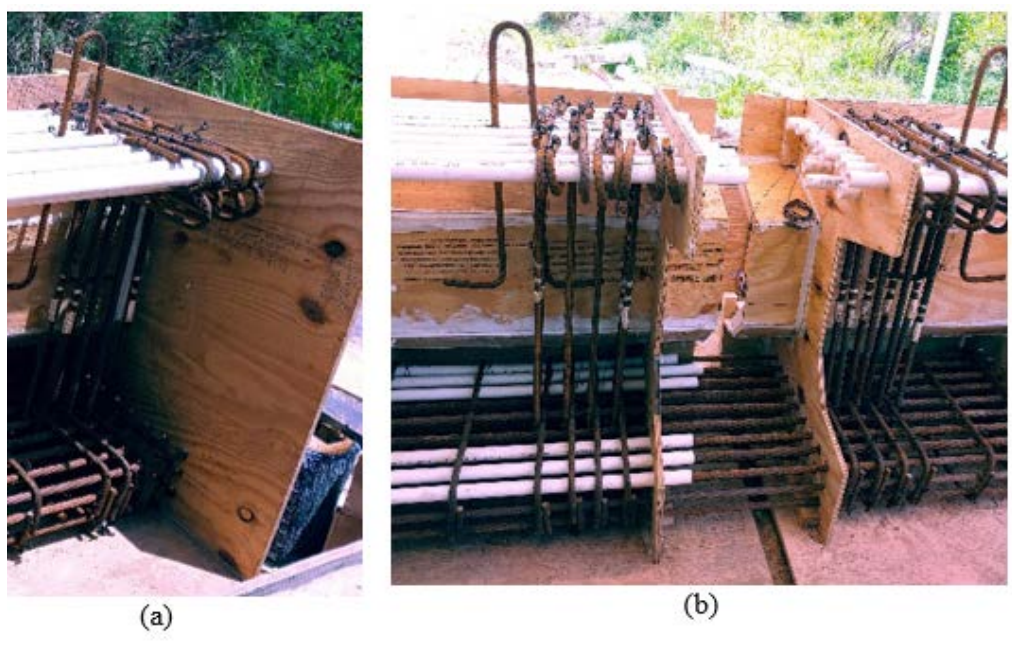


Figure 4-7: Reinforcement details at girder ends. (a) Girder A end. (b) Ends between Girders A & B.

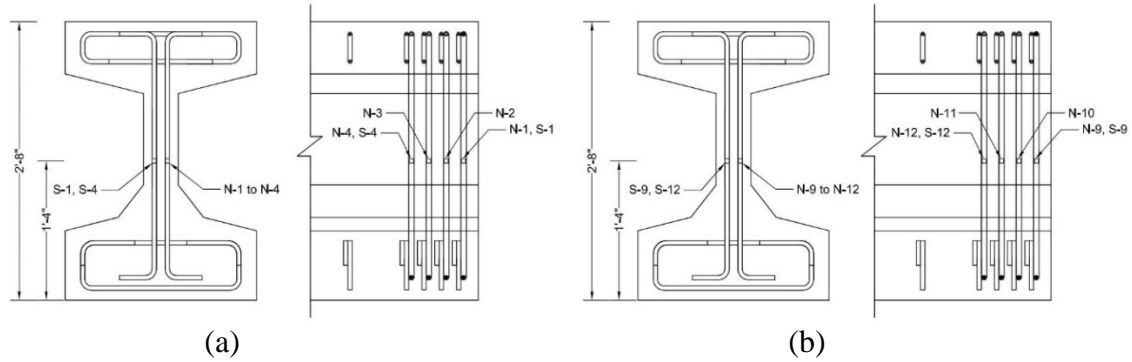


Figure 4-8: Strain gauge locations on web reinforcement. (a) Girder A. (b) Girder B.

4.2.2 Prestressing Strands

Figure 4-9 shows that the bottom strands were pretensioned using a monostrand jack. Each strand was fully tensioned to 202.5 ksi, or 43.9 kip. The strands were tensioned symmetrically from the center to exterior columns at individual layers. The bottom strands were cut using an acetylene torch when the UHPC achieved a compressive strength of 13.0 ksi. **Figure 4-10** shows a side view of Girders A and B after the release of the bottom strands. Similarly, the top strands were post-tensioned to 43.9 kip each symmetrically from the center to exterior columns for simplicity (**Figure 4-11**). Due to the limited availability of bearing plates for chucks, some top strands in Girder A were partially stressed, equivalently to 4 and 3 fully prestressed strands at the upper and lower layers, respectively. All 9 top strands in Girder B were fully post-tensioned. After all strands were prestressed, no visible cracks were observed at the girder ends (**Figure 4-12**).



Figure 4-9: Pretensioning bottom strands.



Figure 4-10: Side view of Girders A & B.



Figure 4-11: Post-tensioning of top flange steel strands.



Figure 4-12: End of Girder A after all strands were prestressed.

4.2.3 Strain Readings

A total of 6 strain gauges were installed at four pairs of web reinforcement at one girder end (see **Figure 4-8** for gauge locations). Strain gauge readings were collected when the bottom strands were cut, and the top strands were post-tensioned. **Figure 4-13** to **Figure 4-16** show the readings of the strain gauges in the web reinforcement at one end of Girders A and B. As illustrated in **Figure 4-13**, strain gauge readings versus time were reported after release of bottom strands in Girder A. Steel strains were 95 and 124 microstrain at N-1 and S-1 gauges, respectively, which were mounted to the first pair of bars closest to the girder end. The tensile strains in web reinforcement rapidly reduced when the reinforcing bars were away from the girder end. Similar plots were provided in **Figure 4-14** for Girder A when the top strands were post-tensioned. **Figure 4-15** and **Figure 4-16** illustrate the gauge readings in Girder B when the bottom strands were released and when the top strands were post-tensioned, respectively.

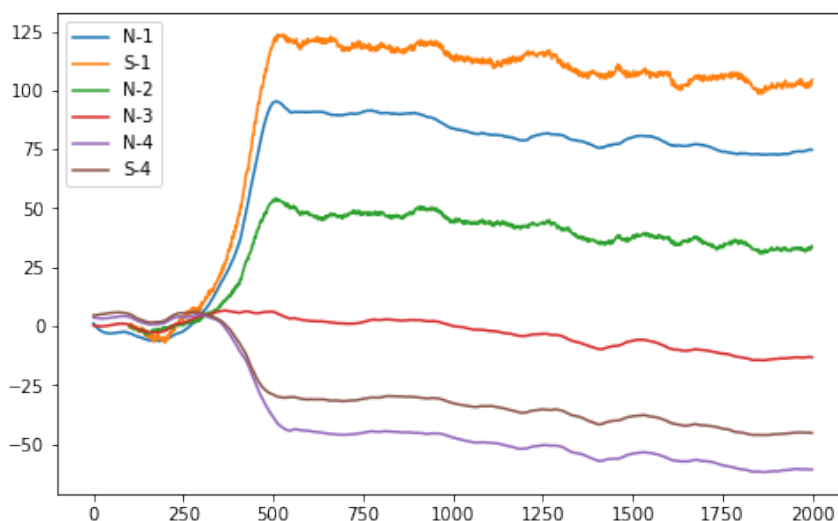


Figure 4-13: Girder A rebar strain (microstrain) vs. time (second) plots at release of bottom strands.

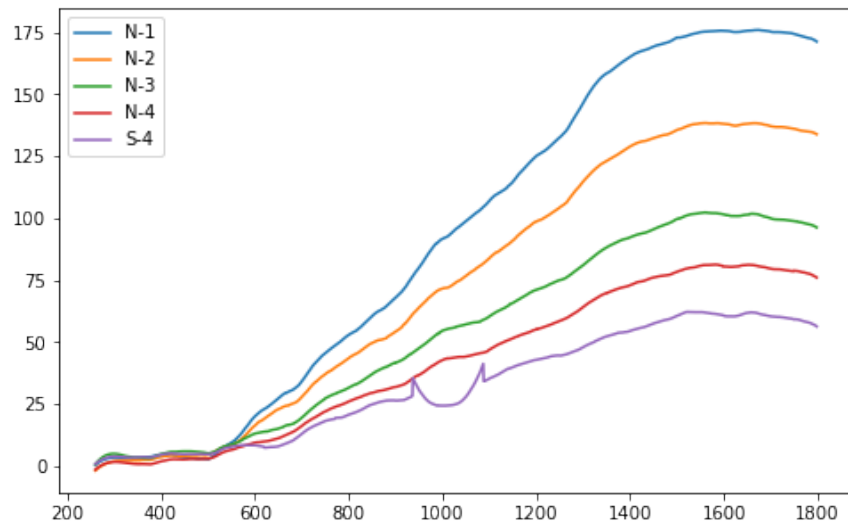


Figure 4-14: Girder A rebar strain (microstrain) vs. time (second) plots after PT top strands.

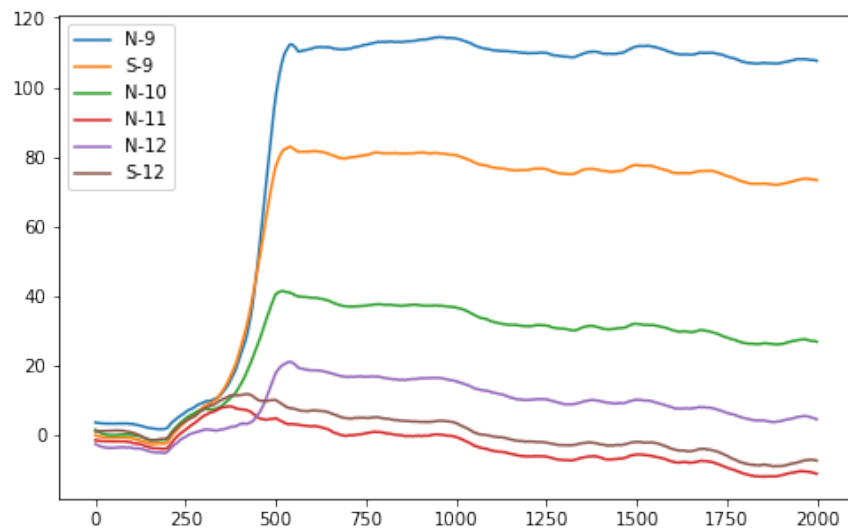


Figure 4-15: Girder B rebar strain (microstrain) vs. time (second) plots at release of bottom strands.

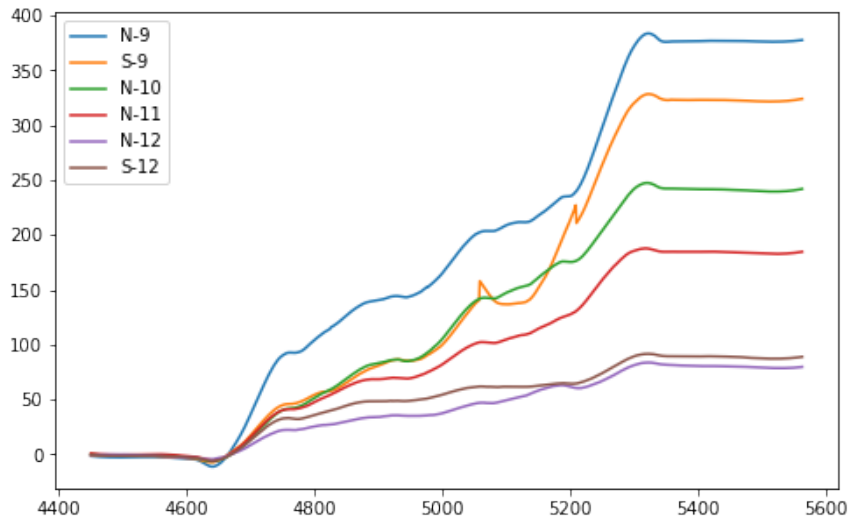


Figure 4-16: Girder B rebar strain (microstrain) vs. time (second) plots after PT top strands.

The strain readings in the web reinforcement were converted to stresses and forces, as summarized in **Table 4-1**. The steel stresses ranged from 2.2 to 8.3 ksi and 3.0 to 13.2 ksi at Girders A and B, respectively. The steel strain versus location of measurement from girder end was plotted in **Figure 4-17**, showing a gradual decrease in strain when the bars were located further away from the girder end. The peak gauge readings were captured after prestressing forces at top and bottom strands were introduced to the girders, which slightly amplified the splitting forces because the prestressing operations were conducted at different times and the gauge readings marginally dropped during the time intervals due to prestress losses. Similarly, **Figure 4-18** shows the variation of steel force versus its location away from the girder end.

Figure 4-19 illustrates the total bursting forces at the girder ends attributable to both UHPC and reinforcement. Two sets of data were plotted assuming 0.75 ksi and 1.0 ksi for average tensile strengths of UHPC, respectively. The bursting resistance due to UHPC was conveniently determined assuming an average tensile strength within a

distance equal to one-fourth of the girder height. **Figure 4-19** also includes three lines corresponding to various ratios, 2%, 3%, and 4%, of splitting forces with respect to the applied prestressing forces due to bottom strands only and total strands. It was found that the ratios based on the test results varied from 2% to 4%.

Table 4-1: Collected strain readings and calculated stresses and forces in the reinforcement.

Girder No.	Rebar location from girder end (in.)	Strain (microstrain)	Stress (ksi)	Force (kip)	Total force (kip)
A	1 ½"	285	8.3	5.1	11.9
	3 ½"	192	5.6	3.5	
	5 ½"	109	3.2	2.0	
	7 ½"	77	2.2	1.4	
B	1 ½"	455	13.2	5.3	12.1
	3 ½"	289	8.4	3.4	
	5 ½"	196	5.7	2.3	
	7 ½"	104	3.0	1.2	

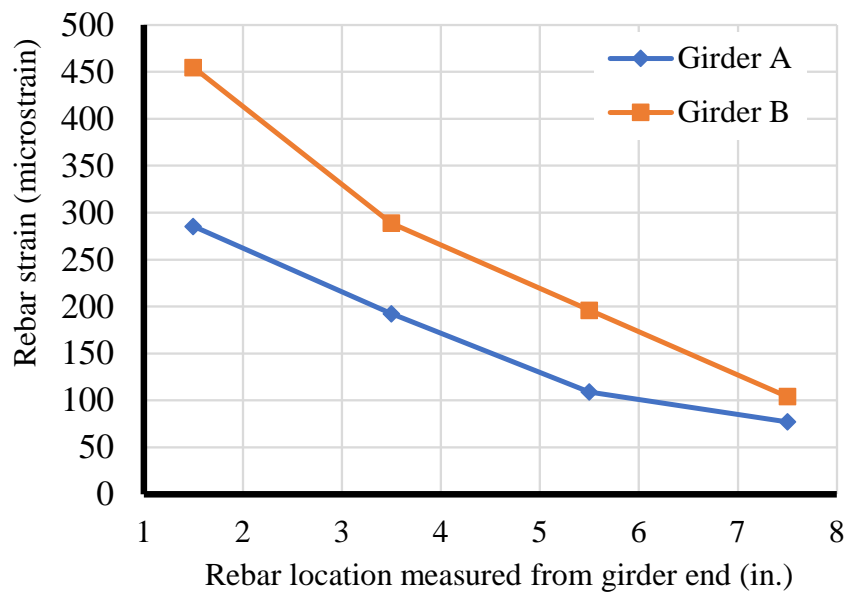


Figure 4-17: Variation of rebar strains vs. locations.

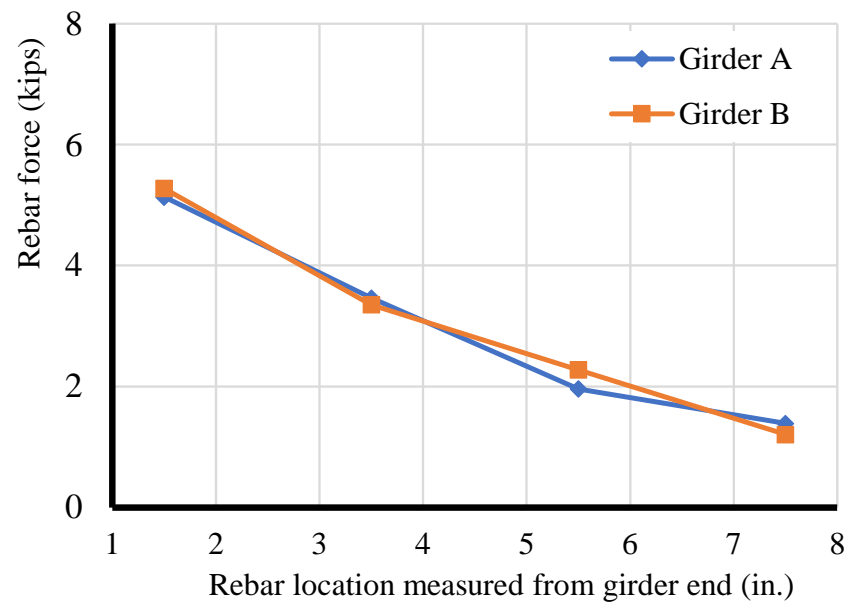


Figure 4-18: Variation of rebar forces vs. locations.

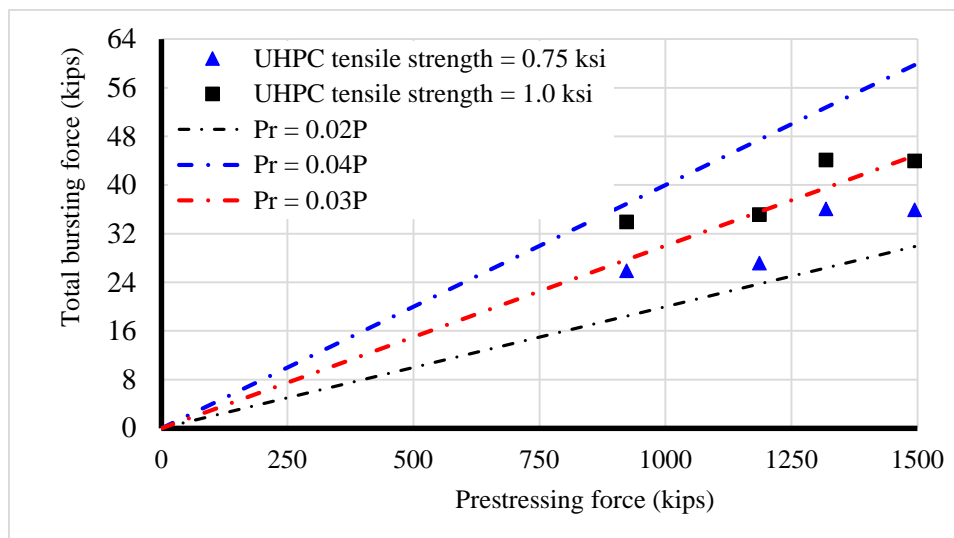


Figure 4-19: Resulting bursting forces at girder ends.

4.3 Gergely-Sozen Analysis

Computations for the Gergely-Sozen analysis were performed for Girders A and B. The analyses reported the end zone responses subject to both pretensioning and post-tensioning strands. In **Figure 4-20** and **Figure 4-21**, the variation of the moment along the depth of the cross section at the girder ends are shown. The depth is measured from the girder bottom. The magnitude of the moment in the girders at both girders was found to be similar with Girder B being slightly higher even though it had less strands. This results from the fact that moment distribution not only depends on the applied prestress force, but the strand pattern. A summary of the findings is outlined in **Table 4-2**, in which the bursting force is seen to be about 5% of total prestressing force, indicating the conservative nature of this method. This method was developed assuming that concrete cracks and vertical reinforcement carries all splitting forces, however, UHPC is known to exhibit post-cracking strength.

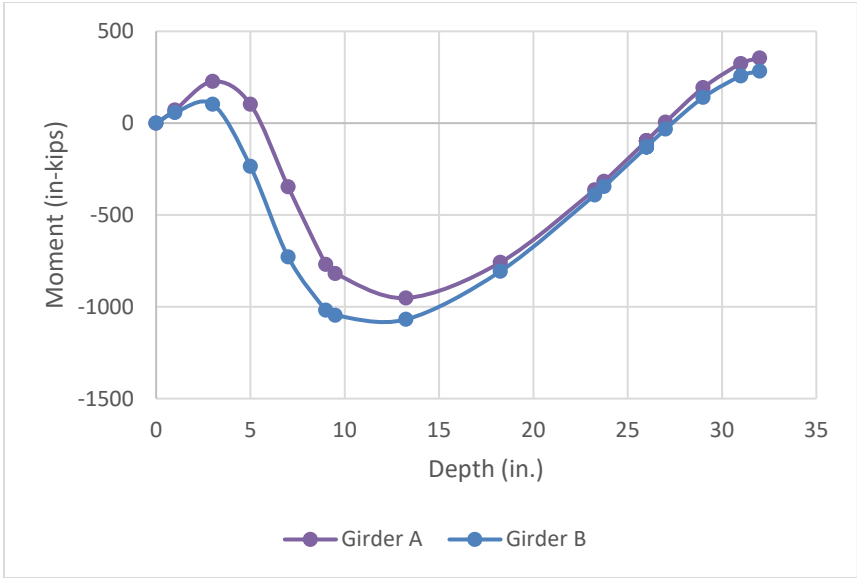


Figure 4-20: Moment diagram at the end zone of Girder A and B due to pretension.

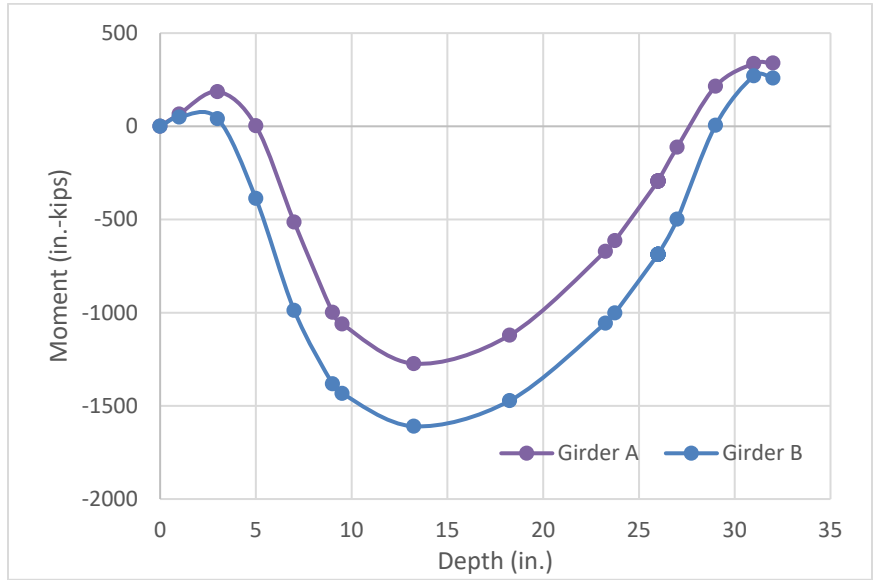


Figure 4-21: Moment diagram at the end zone of Girder A and B due to prestressing.

Table 4-2: Summary of Gergely-Sozen analysis.

	Pretension		Full Prestress	
	Girder A	Girder B	Girder A	Girder B
Moment (in.-k)	-952.34	-1068.96	-1273.48	-1609.82
Bursting Force (kip)	39.68	44.54	53.06	67.08
P (kip)	1186.45	922.79	1494.05	1318.28
% of P	3.34	4.83	3.55	5.09

4.4 Numerical Analyses

Numerical analyses are performed when there is no close-form analytical solution to the problem of interest. Additionally, in several cases, the cost of experimental setups in terms of materials or efforts becomes excessive. Hence, finite element (or finite difference) analysis of such a problem becomes a viable option as a stand-alone effort or combined with experimentation.

There is optimism that the cost of UHPC will become more affordable as industry adoption increases and non-proprietary mix designs become widespread. However, as this is not the current situation, we performed numerical analysis in this research to gain additional insight from the experimental setups. The models were validated and calibrated with the experimental findings. This section describes aspects of the analysis relating to the development of the models as well as the results obtained from ANSYS Mechanical 2020 R2.

4.4.1 Material Models

The mechanical behavior of UHPC, steel tendons, and end zone reinforcement used in the simulation is defined by material models. The appropriate models were selected for each material based on our requirements and the limitation(s) of each model.

Concrete material models in ANSYS include the Microplane, Menterey-Williams, and Drucker-Prager Concrete (DPC), all of which are non-linear material models that capture the non-linearity of concrete behavior. Neither of these models can present a concrete cracking visualization in the same way that the now-deprecated concrete models (TB, CONCR) did. They are, however, not as susceptible to analysis convergence and mesh sensitivity issues that faced the legacy model.

Microplane model is based on the concept of discretizing the problem domain by microspheres each with a pair of 21 microplanes that determine its interactions with neighboring spheres. The stress-strain relationships are defined on these microplanes. This material model has been shown to have lesser convergence issues. However, it was incompatible with the approach we adopted for modelling the prestress in the steel strands and thus could not be used. Hence, the Drucker-Prager Concrete (DPC) Model was adopted.

The Drucker-Prager Concrete (DPC) model in ANSYS is a rate-independent viscosity model that extends the typical single-surface Drucker-Prager model. DPC captures the difference between tensile and compressive behavior in concrete. Parameters were inputted for the yield surfaces as well as the Hardening Softening and Dilation (HSD). The primary elastic properties defined were:

- Density: 155 lb/ft³

- Modulus of elasticity: 5587 ksi
- Poisson ratio: 0.2

DPC model parameters presented in **Table 4-3** are based on the stress-strain relationship shown in **Figure 4-22**, in which compression behavior is taken as linear until 70% of the uniaxial compressive strength of concrete f'_c . A more complex behavior was defined in tension, which was simulated by opting for the steel reinforcement Hardening Softening and Dilation (HSD) presented in **Table 4-4**.

Table 4-3: Drucker-Prager concrete model constants.

Property	Symbol	Value
Uniaxial compressive strength	R_c	13.0 ksi
Uniaxial tensile strength	R_t	1.5 ksi
Biaxial compressive strength	R_b	18.0 ksi

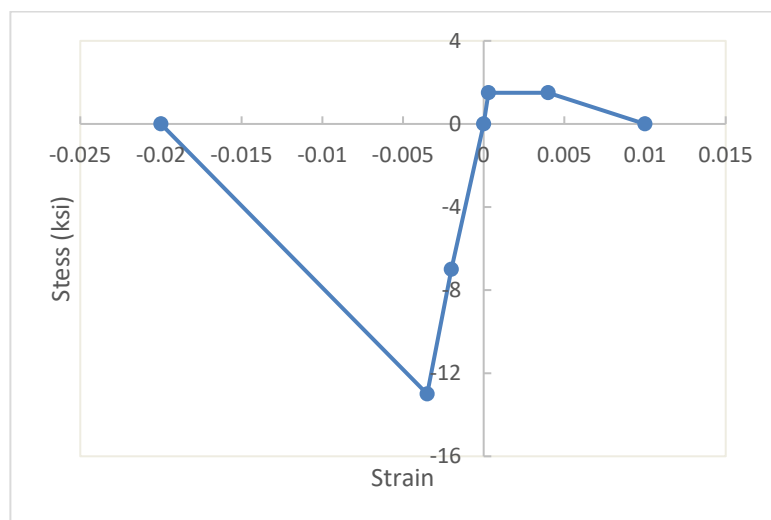


Figure 4-22: Typical stress-strain relationship for UHPC

Table 4-4: HSD parameters.

Category	Property	Value
Softening	Plastic strain at uniaxial compressive strength	0.0035
	Relative stress at onset of nonlinear hardening	0.7
	Residual compressive relative stress	0.001
	Softening plastic strain point 1	0.002
	Softening plastic strain point 2	0.004
	Softening plastic strain point 3	0.01
	Residual tensile relative stress point 1	1
	Residual tensile relative stress point 2	0.001
	Residual tensile relative stress point 3	0.001
	Initial tensile dilatancy parameter	0.75
	Tensile dilatancy parameter point 1	0.75
	Tensile dilatancy parameter point 2	0.75
	Tensile dilatancy parameter point 3	0.75
	Dilatancy	Tension Tension-Compression Dil.
Compression Dilatancy		1

Grade 270 low-relaxation strand material model follows the Power Equation describing the non-linear behavior of the strands (Devalapura et al. 1992). **Eq. 4-1** below shows the power equation and **Figure 4-23** gives a visualization of this stress-strain relationship. However, for computational efficiency, the Power Equation was dropped in favor of the Bilinear model, which the plot shows as a good substitute.

$$f_s = E_s \varepsilon_s \left[Q + \frac{1 - Q}{\left[1 + \left(\frac{E_s \varepsilon_s}{K f_{py}} \right)^R \right]^{\frac{1}{R}}} \right] \leq f_{pu} \quad \text{Eq. 4-1}$$

Bilinear model with parameters $f_y = 243 \text{ ksi}$, $E = 28500 \text{ ksi}$ and *Tangent Modulus* = 1459.46 ksi was used to approximate the steel tendons. An additional bilinear model was also defined to represent the ASTM A615 reinforcement bars in the end zone. The material model parameters were $f_y = 60 \text{ ksi}$, $E = 29000 \text{ ksi}$ and *Tangent Modulus* = $E/1000 = 29 \text{ ksi}$. The particular value of tangent modulus did not matter since we expected no yielding in the rebars.

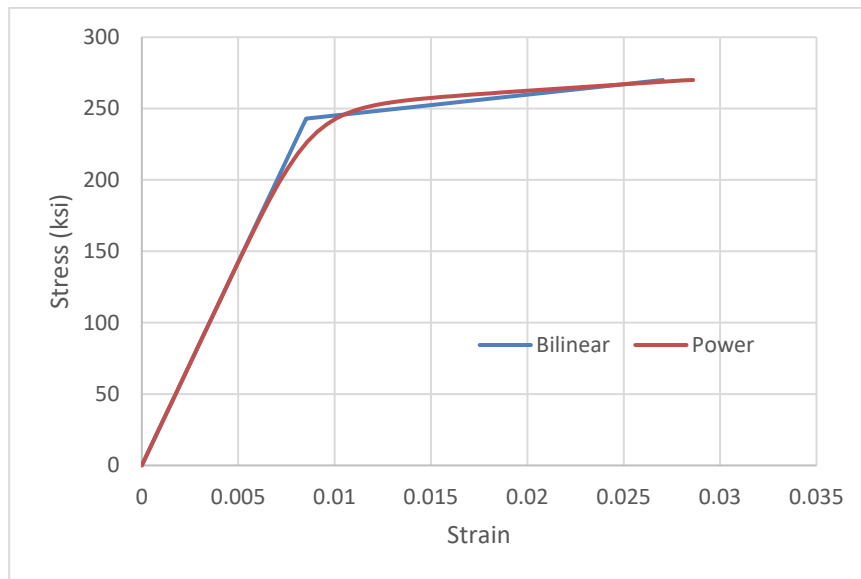


Figure 4-23: Stress-strain relationship of steel strand.

4.4.2 Elements Technology and Meshing

Similar to the material models, the element types selected for each part of the model were different and based on geometry of the part as well as the material model requirements. LINK180 elements are linear, 1D truss elements with only two nodes that

resist load only in tension or compression but not flexure. These were used to model both reinforcing bars and strands. It supports defining initial stress which was used to define the prestressing.

SOLID185 elements were selected for the UHPC. This is a linear, 3D, brick element with eight nodes suitable for the solid nature of UHPC and supports the DPC material model. See **APPENDIX A** for ANSYS APDL commands invoked to merge the coincident nodes of the link and solid elements as well as defining prestressing.

4.4.3 Verifications

Despite several published studies on the end zone behavior of conventional prestressed concrete girders, only a few are on UHPC girders as it is a relatively newer material. Even fewer of these studies are on the numerical analysis of such UHPC girder behavior. However, Chen & Graybeal, (2012) performed and published their studies on numerical analysis of their previous flexure and shear tests of prestressed UHPC girders (Russell et al., 2013).

Verification of FHWA Flexural Girder

The test of interest was beam 80F of which a quarter model was created in ANSYS using the material properties provided in their published work. Material properties were inputted into the earlier discussed DPC model in ANSYS. Two load steps were created, the first for the prestressing, and the second for the vertical load application. However, it was noted that despite the quarter model employed to harness the symmetries of the problem domain, this was still a highly demanding computation due to the flexural load step – a behavior which is beyond the scope of our study as presented in subsequent sections.

Comparing the load-deflection curve shown in **Figure 4-24** between ANSYS, testing, and the other numerical studies performed by the authors, a strong agreement was overserved in the linear elastic region as well as in a partial nonlinear region. **Figure 4-25** also shows a similar agreement to the midspan top and bottom strains of the girder.

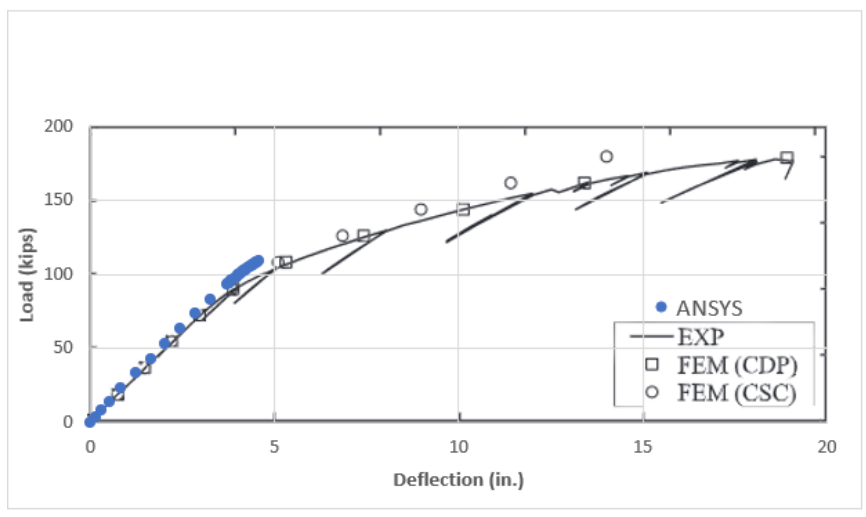


Figure 4-24: Load-deflection comparison.

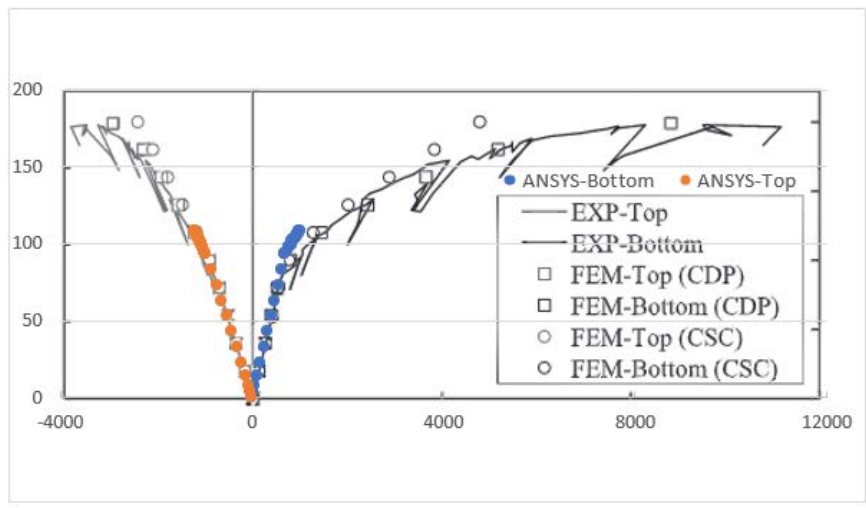


Figure 4-25: Longitudinal strain comparison.

The ANSYS verification model terminated before reaching the ultimate failure as the figures show but fully captures the cracking and nonlinear behavior of concrete. Evidence of this is in **Figure 4-26** which shows the stress-strain plot of bottom fiber of the girder as loading progressed. The softening behavior implemented to simulate concrete commenced at the yield stress as expected. This is further highlighted in the stress contours shown in **Figure 4-27**, showing the yielding/cracking region (in red) starting to extend beyond the bottom flange. Beyond this load, the model would have proceeded to experience the excessively large tensile strains reported in the original test data and then failed.

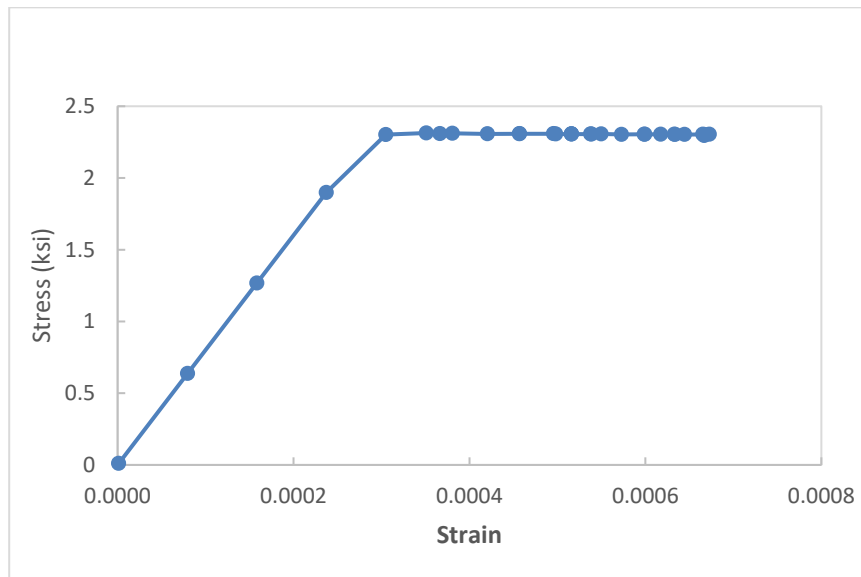


Figure 4-26: Tensile stress-strain behavior of ANSYS DPC model.

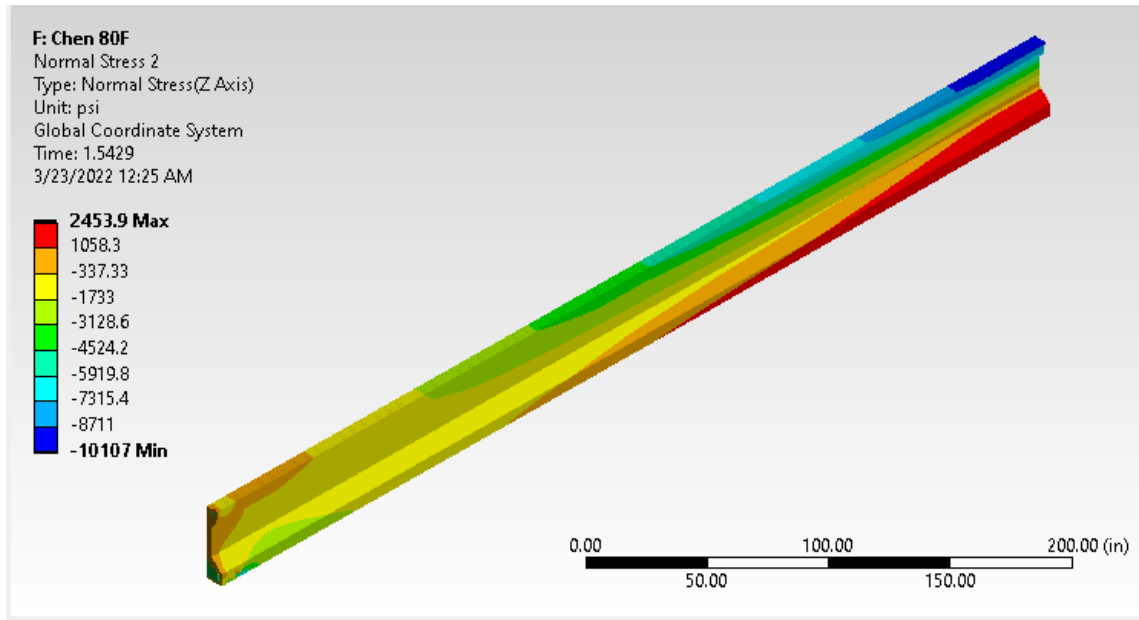


Figure 4-27: ANSYS stress contour at 119 kip loading.

Verification of FHWA End Zone Girder

Mohebby et al. (2019) published their findings on UHPC girders that they had tested. The girders as shown in **Figure 4-28** were 35 in. deep and 26 in. wide featuring a 3 in. web thickness. A total of 26 0.7 in.-diameter low-relaxation strands were provided and each strand applied 57.5 kip of prestressing force. Bundled pairs of #5 reinforcement bars spaces at 3 in. were provided in the end zone. All the details about geometry, material, and prestressing from their work were incorporated in an ANSYS model.

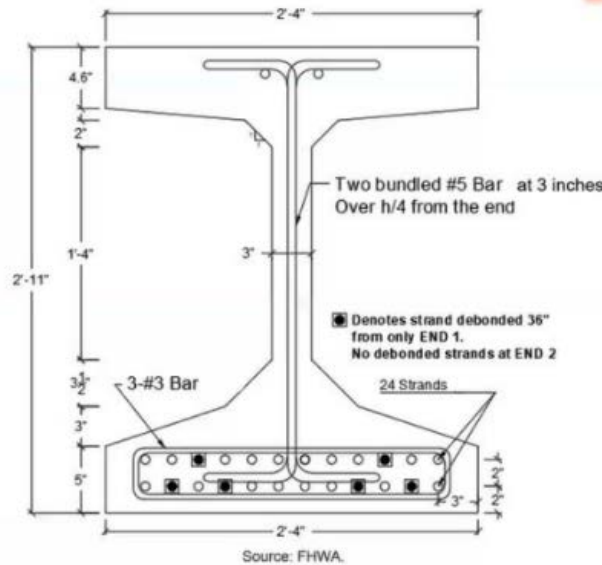


Figure 4-28: Details of girder tested by FHWA.

Bursting stress contour output from ANSYS is shown in **Figure 4-29**, it is evident that there is bursting force in the web that led to the tensile stress in the UHPC and at some locations the limit was reached. A comparison of the stress in the reinforcement bars was made and presented in **Figure 4-30**. Relating ANSYS to test Girder A, we observe a slightly higher tensile stress in the rebar closest to the end of the girder. There is a strong agreement at the other reinforcement locations. UHPC stress was extracted for the ANSYS model for comparison with test analysis those authors performed as shown in **Figure 4-31**. ANSYS showed slightly lesser values, however, there is a strong similarity in trend. From the ANSYS model, the bursting force resisted in the end zone was 57.8 kip (24.2 kip and 33.6 kip by steel and UHPC respectively). This is comparable to the test analysis which gave 62.1 kip (21.6 kip and 40.5 kip by steel and UHPC respectively).

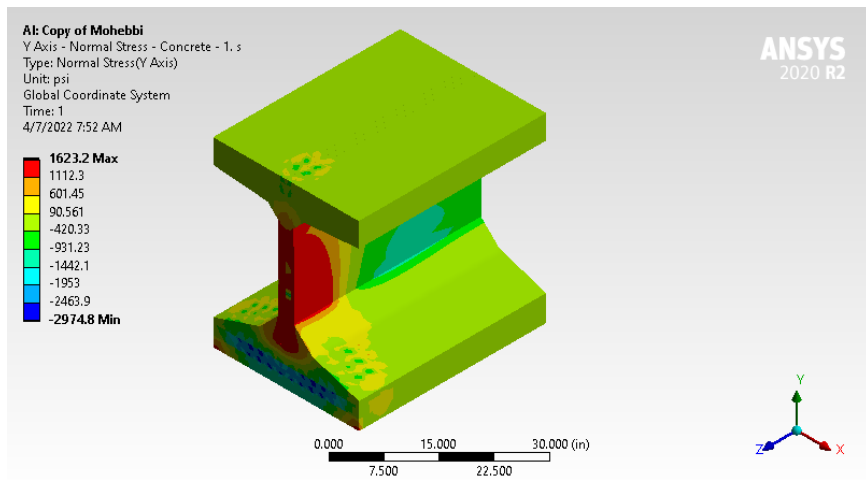


Figure 4-29: Bursting stress contour of FHWA girder.

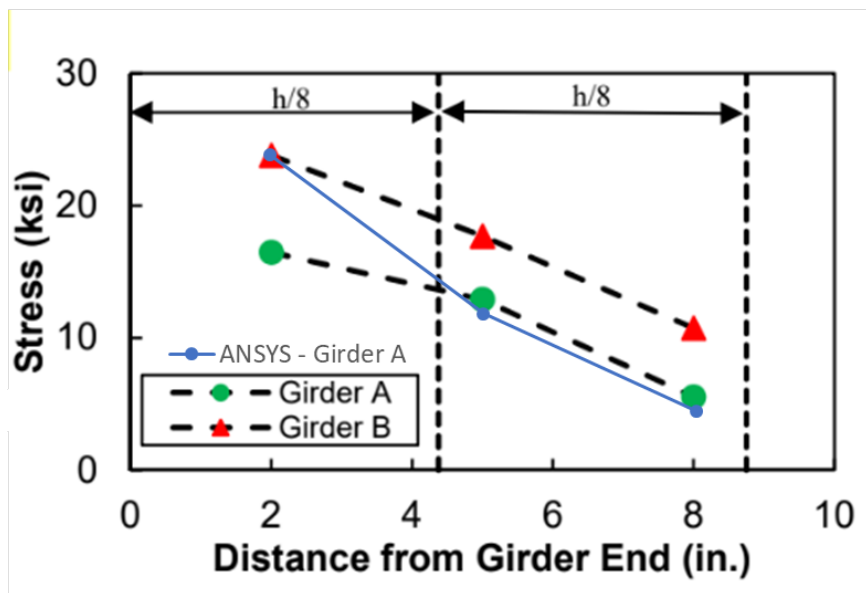


Figure 4-30: Comparison of stress in reinforcement bars.

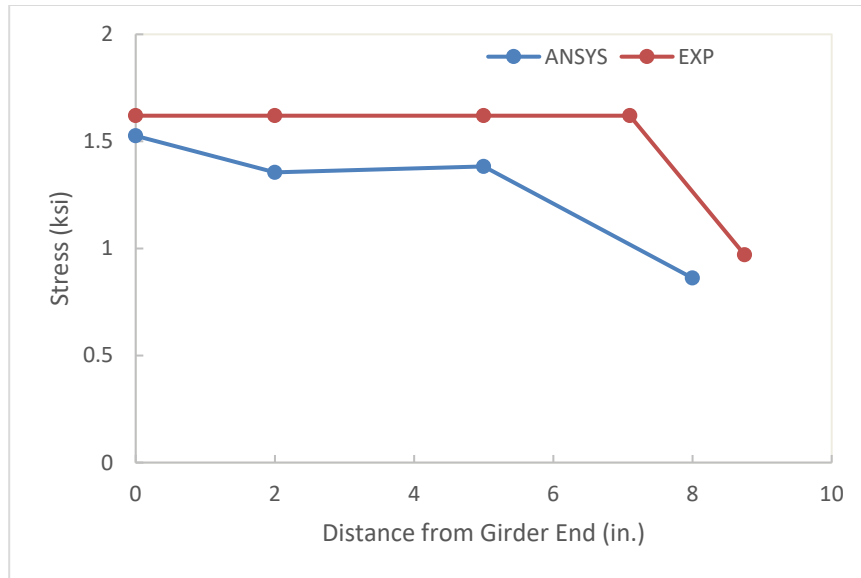


Figure 4-31: Comparison of stress in UHPC.

4.4.4 Girders A and B

The material models described earlier in Section 4.4.1 along with the geometry details of the test girders discussed in Section 4.2 were incorporated into the two Static Structural Analysis models using ANSYS Mechanical for Girders A and B. The symmetry of the problem domain justified modeling half of the girder along its length. At the location of the symmetry plane, the model was prevented from longitudinal translation, while at the free end, the only constraint was on vertical translation as illustrated in **Figure 4-32**.

In general, 3D 8-node linear tetrahedral elements (SOLID185) were employed for the UHPC. While for both strands and reinforcing bars, 1D 2-node linear truss elements (LINK180) were applied. The global mesh size was 1 in. and the rebars and strands were meshed to provide nodes that were coincident with that of the UHPC. These shared nodes were then constrained together to represent the bond between the UHPC and

reinforcement. The prestressing effect in the strands was defined as tensile stress using INISTATE commands.

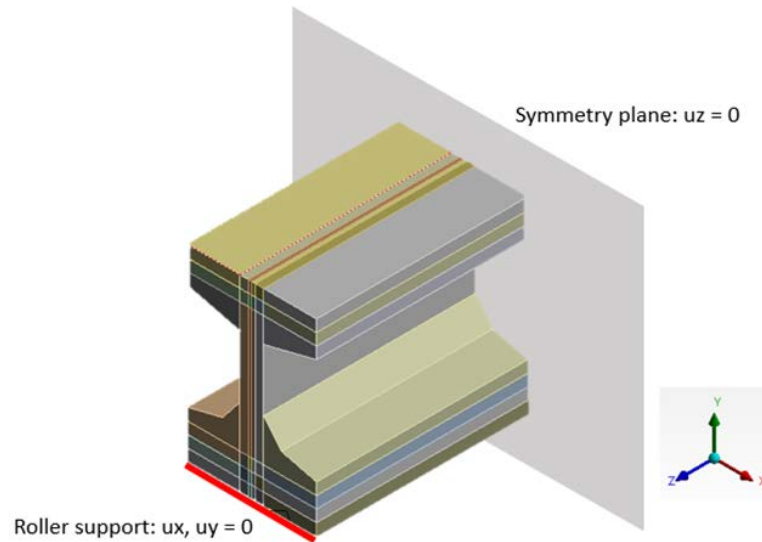


Figure 4-32: Boundary conditions of ANSYS model.

Sensitivity Studies

The response of the model depends on several factors chief among which are the material model and mesh size. Hence, sensitivity studies were performed to eliminate unwanted behavior in the model that could distort the desired comparison. The model on Girder A subject to release of pretensioning strands was developed for this exercise.

Both linear and nonlinear models on UHPC were generated to study of their effects on the end zone behavior. **Figure 4-33** shows the variation of the stresses at the mid-height of the rebars in the end zone. Both models exhibited a same trend of the stress variation, i.e. the stresses decreased as the distance from the girder end face increased, while the rebars in the linear elastic model carried lower stresses implying that the concrete contributed more to the splitting resistance. This is exactly what it is evident in the bursting stress contour found in **Figure 4-34**. The concrete stress is unreasonably

high, over 4 ksi, exceeding the specified 1.5 ksi limit significantly. This is due to lack of softening (or cracking) in the linear model. Hence, the nonlinear DPC model is more appropriate for this study where concrete cracking is of interest.

Finite element analysis involves the discretization of the problem domain into small, connected elements. The size of these elements affects the accuracy of the model, which is even more critical in the case where nonlinear behavior like cracking is expected. Models were developed using global element sizes of 1 in. and 2 in. to allow for a mesh sensitivity study, as summarized in **Figure 4-35**. It revealed that both mesh sizes resulted in comparable stresses in the reinforcing bars except at the first bar, in which the 1 in.-mesh size slightly lowered the stress. The 1 in.-element size was eventually adopted without incurring prohibitive computational costs.

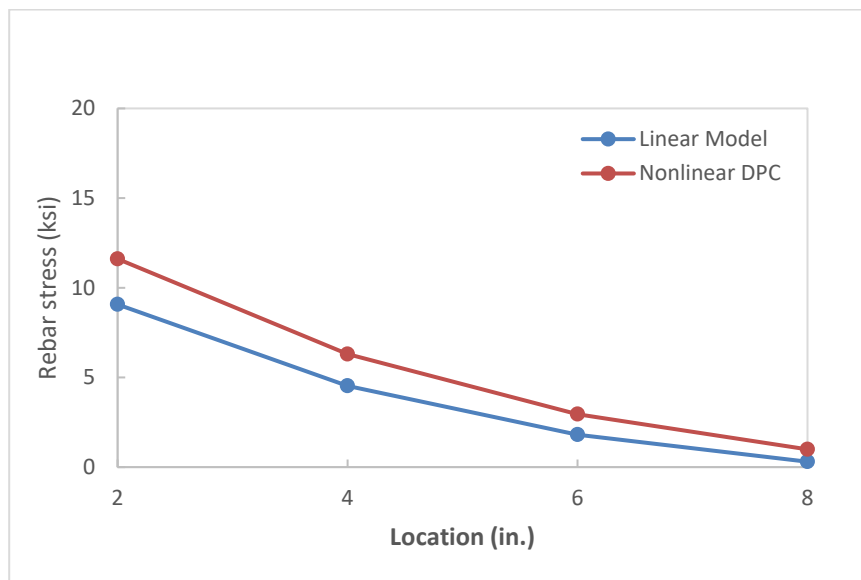


Figure 4-33: Effect of UHPC material model.

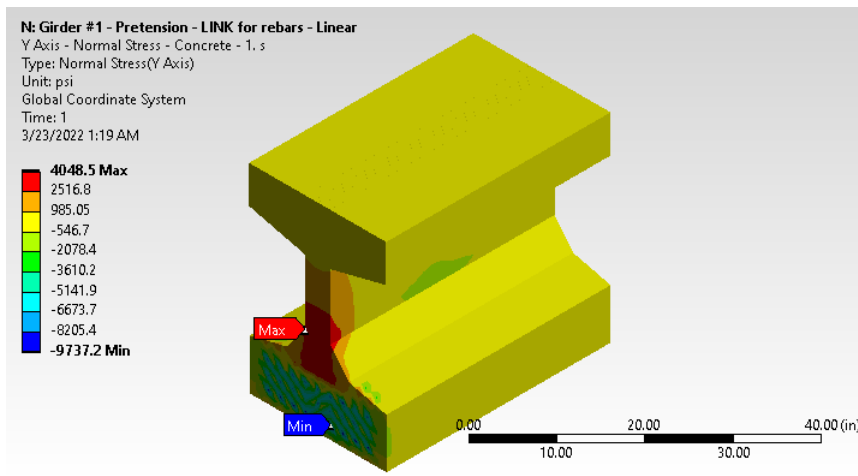


Figure 4-34: Contour of bursting stresses using linear elastic model.

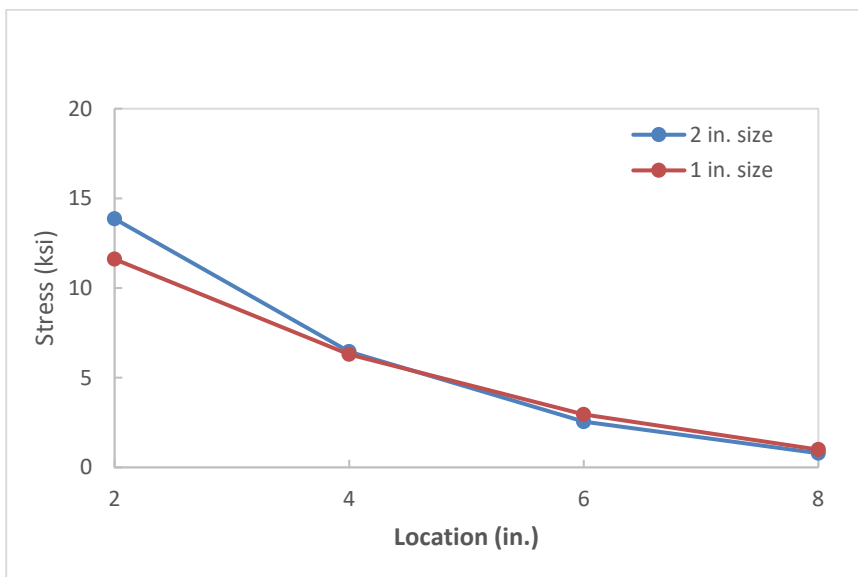


Figure 4-35: Effect of element sizes on rebar stresses.

Results

The visualization of the stress distribution in the end zone reinforcement can be found in **Figure 4-36** and **Figure 4-37** for Girders A and B, respectively. The reinforcement closest to the beam end showed the highest stress at the mid-height approximately. Reinforcing bars in Girder B typically exhibited higher stresses because of the smaller bar size. **Figure 4-38** and **Figure 4-39** show the stresses and corresponding

forces in the reinforcing bars, respectively. Nearly linear variations can be observed as a function of the bar location from girder end for both girders.

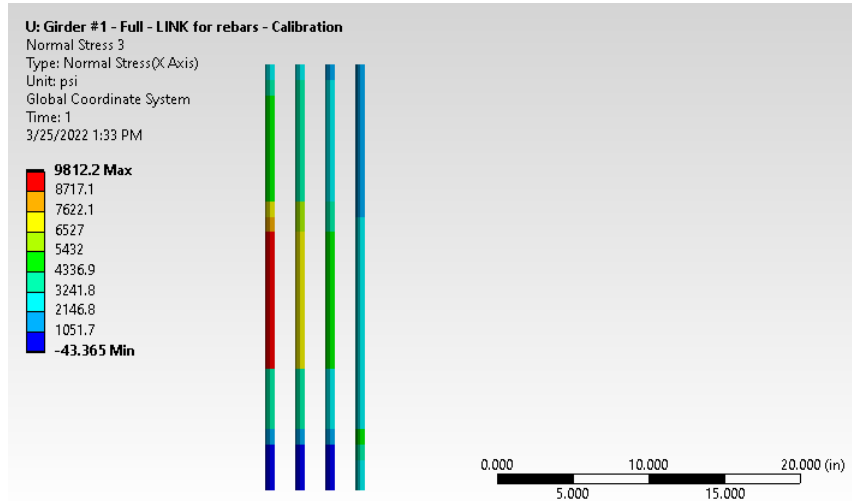


Figure 4-36: Steel rebar stress contour for Girder A.

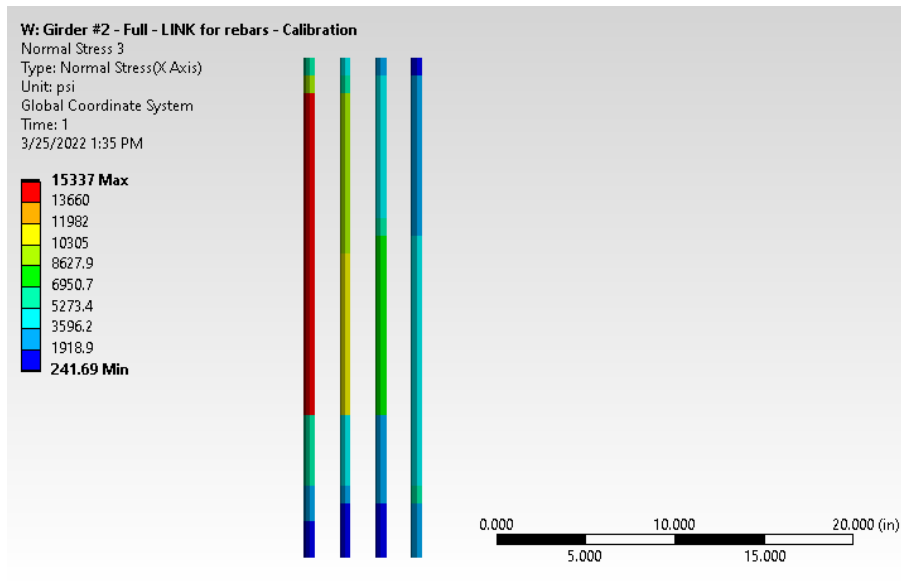


Figure 4-37: Steel rebar stress contour for Girder B.

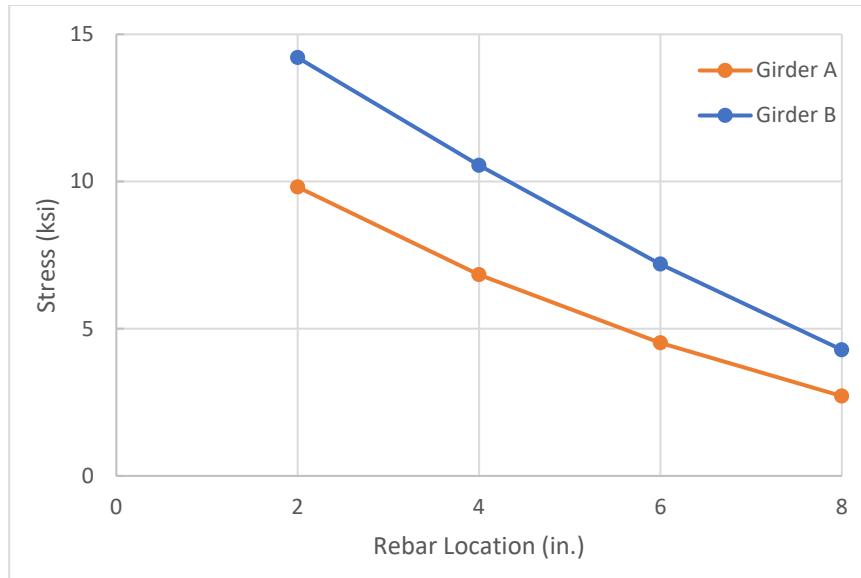


Figure 4-38: Variation of rebar stress corresponding to locations in Girder A.

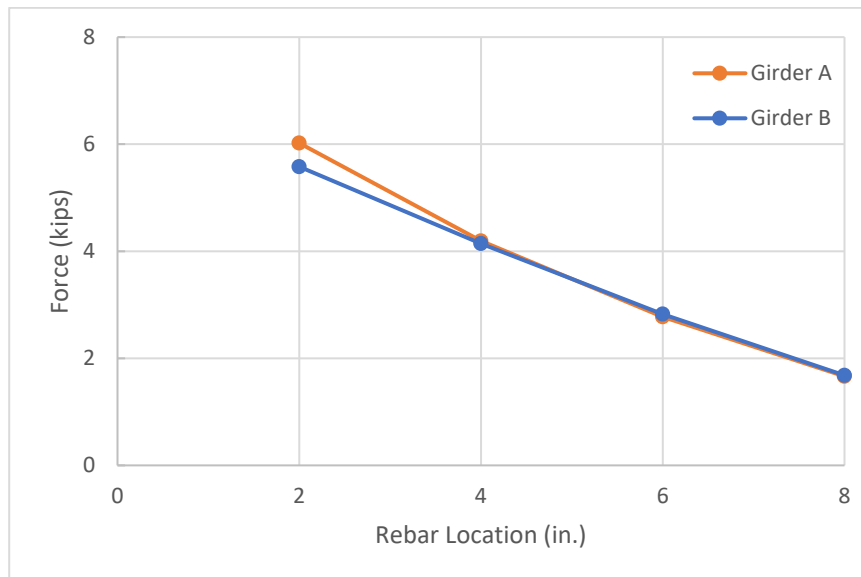


Figure 4-39: Variation of rebar stress corresponding to locations in Girder B.

Even though the ANSYS models provided no visualization of the cracking, we can still draw some insight from the strains plotted in **Figure 4-40** in examining the extent of concrete plastic behavior in the end zone. All models had 1.5 ksi post-cracking strength unless otherwise stated. The UHPC bursting strains at the intersection of the

bottom flange and web is shown in **Figure 4-40**. The appropriate $h/4$ location as well as the cracking strain limit are also displayed. In the Girder B models with 1.0 and 0.75 ksi tensile strengths, the strain did not fall below the limit before $h/4$, indicating a crack length longer than $h/4$, while other cases corresponded a crack length within $h/4$.

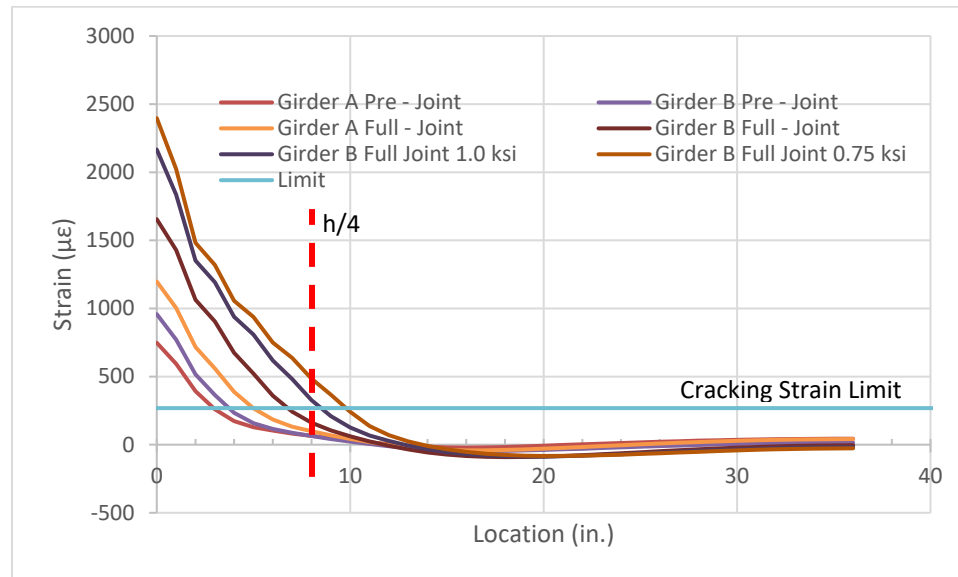


Figure 4-40: Evolution of bursting strains at web-flange interface.

4.4.5 Analysis of a 9 ft-Deep Girder

Tadros et al. (2021) presented a 9 ft-deep, 250 ft-long decked bridge girder design example. This girder bottom flange consisted of 54 pretensioned 0.7 in.-diameter strands at midspan and 46 strands at the ends due to debonding. In addition, there were 14 post-tensioned 0.5 in.-diameter strands at the girder top flange. FEA of the 9 ft-deep girders was conducted to study the effect of the girder depth. **Figure 4-41** details the cross-sectional dimensions of the girder.

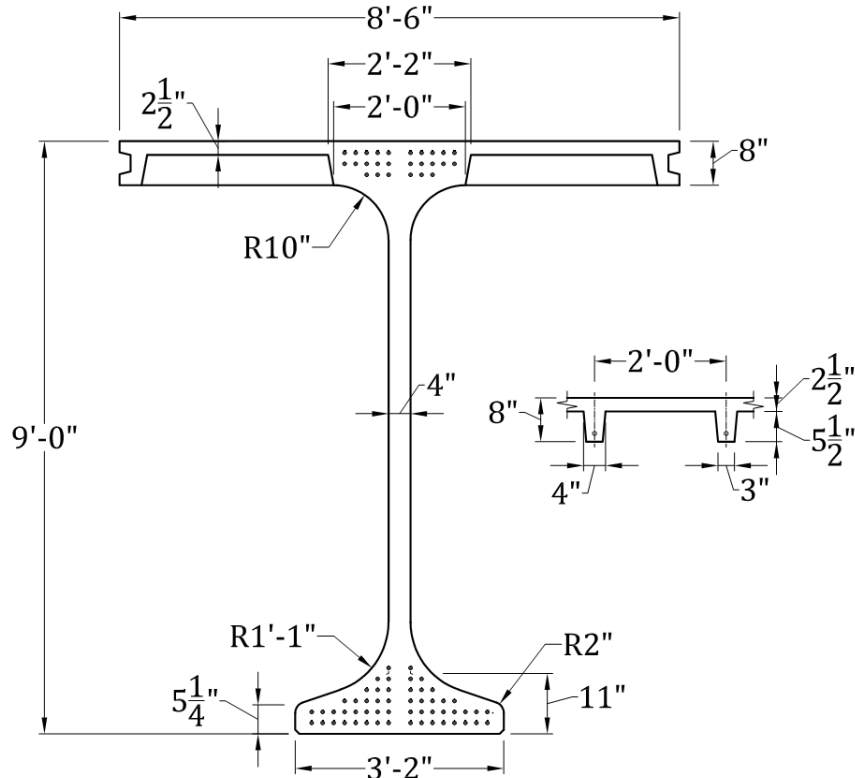


Figure 4-41: Cross-sectional details of a 9 ft deep girder.

The FEA model of the deep girder accounted for a post-cracking stress of UHPC $f_{rr} = 0.75 \text{ ksi}$, as presented by Tadros et al. (2021). The bursting stress in the UHPC at the end zone was assumed to vary from 0.75 ksi to 0 over a distance of $h/4$. The design equation is presented below:

$$P_r \leq f_s A_s + 0.125 f_{rr} h b_v \quad \text{Eq. 4-2}$$

Based on our finite element analyses and experimental study by Mohebbi et al. (2019), the equation below is recommended assuming a trapezoidal distribution for UHPC's bursting resistance:

$$P_r \leq f_s A_s + 0.75 f_{rr} L_{ez} b_v \quad \text{Eq. 4-3}$$

Where L_{ez} is the effective length of the splitting resistance due to UHPC and reinforcing bars, measured from the end of the girder, which is either $h/8$ for deeper girders or $h/4$

for shallower sections. FEA models were created using the amount of splitting reinforcement using the proposed equation. **Table 4-6** summarizes the parameters in the deep girder study. The one-legged steel reinforcements provided at 10 locations were spaced at 3 in. and the first bar was located 1 in. from the girder end for $h/4$ models. However, the layout for $h/8$ models used one-legged of 6 bars with a 3 in. spacing and the first bar was 1 in. from the girder end. The bars had the same cross-sectional area.

Case 1 is based on Tadros' equation presented earlier and case 2 is based on the proposed equation. Case 3 model retained the exact area of steel obtained from case 2 but assumed 1.5 ksi for UHPC's post-cracking strength. The models in cases 4 and 5 investigated the appropriateness of taking $h/8$ for L_{ez} of deep girders for post-cracking of 0.75 ksi and 1.5 ksi, respectively. Case 6 model contained three times the steel area in case 4.

Table 4-5: Description of modeled deep girders.

Case	End Zone (in.)	UHPC stress block	f_{rr} (ksi)	A_s (in^2)
1	$h/4$	Triangle	0.75	4.40
2	$h/4$	Trapezium	0.75	3.39
3	$h/4$	Trapezium	1.50	3.39
4	$h/8$	Trapezium	0.75	4.91
5	$h/8$	Trapezium	1.50	3.39
6	$h/8$	Trapezium	0.75	14.73

A summary of bursting forces for the models are shown in **Table 4-6**. All bar strains were extracted from the models at the same height where the bar closest to the end experienced the greatest tensile force. UHPC stress/strain outputs were also extracted at

these points. The table also shows the combined splitting resistance from the UHPC and reinforcing bars, as well as the ratios of splitting resistance over applied prestressing forces.

Table 4-6: Bursting forces in deep girders.

Case	Steel (kip)	UHPC (kip)	Total (kip)	% P_{pi}
1	69.23	59.52	128.76	4.07
2	61.16	62.61	123.77	3.91
3	40.06	102.57	142.64	4.51
4	87.68	41.37	129.05	4.08
5	51.06	74.26	125.32	3.96
6	139.70	39.62	179.32	5.66

For the model based on Tadros' equation (Case 1), the model predicted that the total bursting force was 128.76 kip, which was 4.07% of 3215 kip, the initial prestressing force. This was about the same as 128.6 kip bursting force estimated from 4% of the initial prestressing force. It is noticeable that because of the 0.75 ksi limit on the post-cracking strength of UHPC, steel contributed just slightly more to bursting resistance in the breakdown. Despite having slightly less reinforcement in the end zone, the model based on the newly proposed equation (Case 2) had about the same total bursting force. The contribution of steel was still greater than UHPC, however, the difference in contributions was about zero compared to the earlier case.

The total splitting resistance appeared to vary slightly between when 1.5 ksi and 0.75 ksi accounted for the UHPC's post-cracking strength in cases 3 and 2, respectively.

A shift in contribution however occurred for the 1.5 ksi strength because UHPC appeared to provide more resistance than the steel bars.

Cases 4 and 5 sought to address the choice of layout of the reinforcement bars. Model 4 has more steel area packed in a smaller zone than model 2 and a total of 129.05 kip was resisted in bursting and steel contributed the most. Furthermore, model 5 with the 1.5 ksi UHPC post-cracking strength resisted 125.32 kip, but UHPC was the major contributor here. In both models where the end zone was taken to be $h/8$ from girder end, the bursting forces were close to 4% P_{pi} .

The reinforcement level to bring the bar tensile to be less than or equal to 20 ksi was studied in case 6. In all the other cases, **Figure 4-42** shows the stress in the first bar was typically greater than the 20 ksi limit. However, in case 6 where the steel area from case 4 was tripled, the stress level became less than 20 ksi. **Table 4-6** shows that in the case the steel resisted quite a large force compared to UHPC. The bursting force was more than 5%, but this was because the steel area was not based on any design equation requiring 4% P_{pi} initially.

Taking a closer look, consider the distribution of stress in the steel reinforcements as shown in **Figure 4-42** below. In all models, the first location closest to the girder end had the highest stress and there was a gradual decline in subsequent bars. It can be observed that the rebar stresses for these deep girders became quite low at about $h/8$ even for the girders where only $h/8$ was considered as the end zone. In addition, the stress in the first bar for all cases, except 6, was at least 30 ksi which is greater than the 20 ksi allowable limit in the specifications. However, this value was based on crack control in conventional concrete, which may be overly conservative for UHPC girders.

Between cases 2 and 4 where the area of steel increased by about 45%, it is notable that the stress in the first rebar dropped by 18% from 46.32 ksi to 37.99 ksi. In case 6 the stress level became less than 20 ksi because of the large amount of steel reinforcement.

Figure 4-43 shows the forces in the reinforcement bars corresponding to the stresses. The bars in case 6 had the largest forces in comparison to the other cases. There was a general decreasing trend in the forces similar to the stresses.

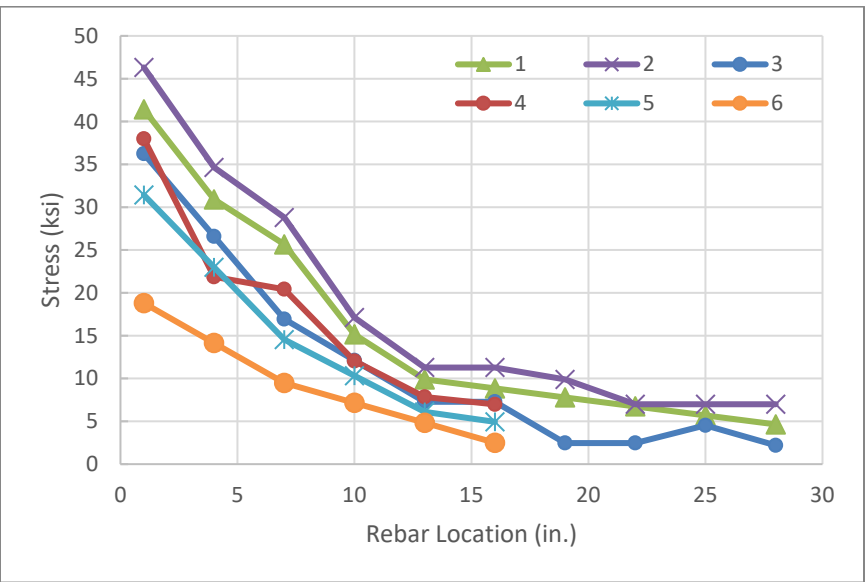


Figure 4-42: Stress in steel reinforcement bars of deep girder.

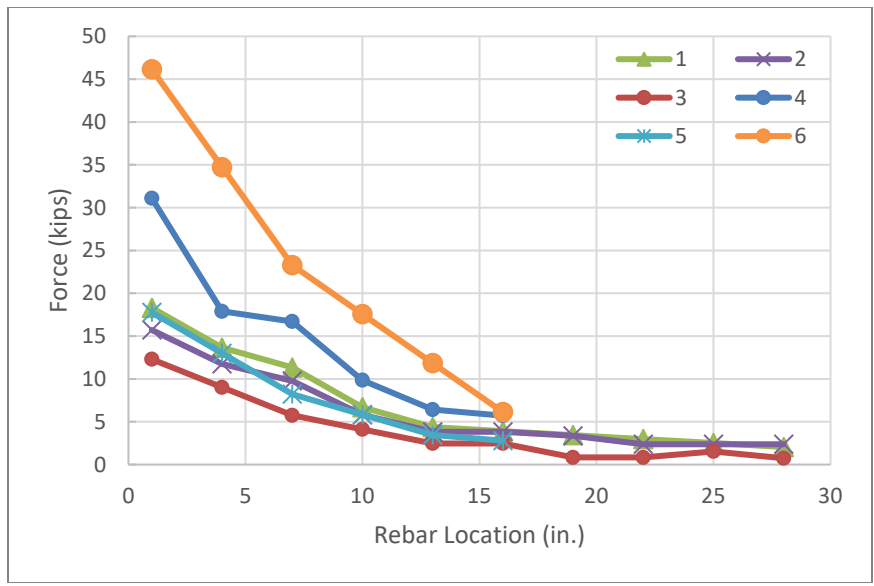


Figure 4-43: Force in steel reinforcement bars of deep girder.

Figure 4-44 shows the distribution of stress in the UHPC at the rebar locations.

Stresses generally stayed constant before dropping off gradually.

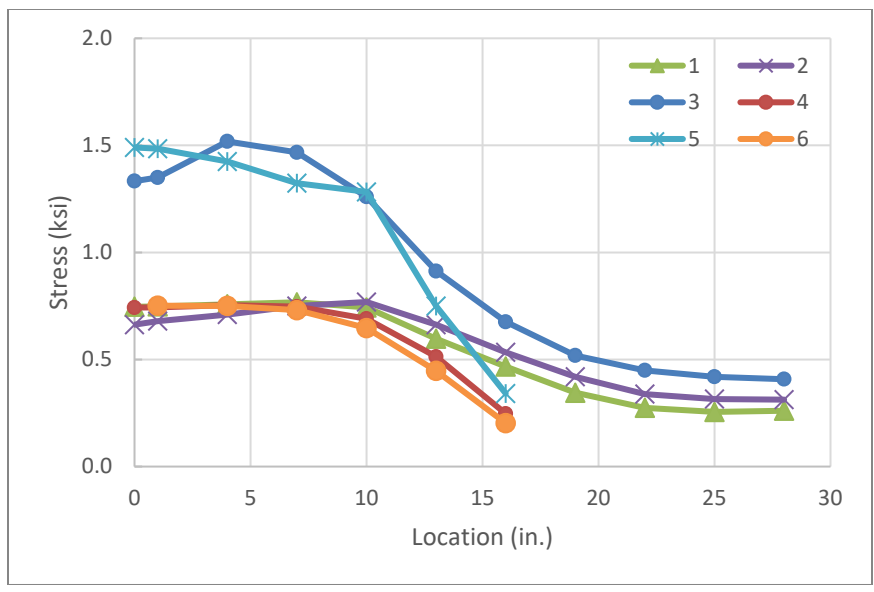


Figure 4-44: UHPC stresses in deep girders.

The stress in the first rebars in **Figure 4-42** all exceed the current 20 ksi limit on steel stress. An investigation into how to lower this stress to the limit was conducted by

solving several models. These are summarized in **Table 4-7** below. Case 1 was exactly the model from case 4 in **Table 4-5** from earlier and was used a baseline for the stress of interest. In case 2, modifications were made to case 1 by starting the first bar at 1 in. instead of 2 in. and the area of steel at this first location was doubled compared to every other location. There about 4 ksi reduction of the stress compared to case 1.

The effect of the location of the first bar was isolated in case 3, which was similar to case 2 except that all reinforcements had the same size. The resulting stress here showed no significant difference from the baseline, implying that the starting locations of the first bar considered had no effect on the maximum stress. Consequently, the stress reduction observed in case 2 was due only to the doubling of the steel area at the first location.

It has been previously established that a higher post-cracking strength reduces the steel stress because the UHPC contributed more to the resistance. Case 4 in **Table 4-7**, which is just like case 3 except that the post-cracking strength is 1.5 ksi, buttresses this trend. There was a 10 ksi reduction in the stress, compared to the baseline case, bringing it close to the 20 ksi limit.

The last case considered featured standard bars sizes. At the first rebar location, which was 1.5 in. from the end, there were 2 bundled #9 bars. At a spacing of 2 in. from this, there were 5 other #7 bars. In effect, there was a drop similar to that occurring in case 4, even though the post-cracking strength was only 0.75 ksi in this case.

Table 4-7: Summary of models studied to lower rebar stress.

Case	f_{rr} (ksi)	A_s (in^2)	Bar size	Spacing	Max stress (ksi)
1	0.75	4.91	6 bars, uniform sizes	3 in spacing, starting @ 1 in.	32.98
2	0.75	4.91	6 bars, 1st double area	3 in spacing, starting @ 2 in.	28.55
3	0.75	4.91	6 bars, uniform sizes	3 in spacing, starting @ 2 in.	32.55
4	1.5	4.91	6 bars, 1st double area	3 in spacing, starting @ 2 in.	23.88
5	0.75	5.00	2 bundled #9 + 5 #7 bars	2 in spacing, starting @ 1.5 in.	24.23

CHAPTER 5

DISCUSSIONS

5.1 Girders Using SMAs

This study explored the feasibility of using SMAs to introduce vertical prestress at a concrete beam end. Small-scale mortar and concrete beams were made involving SMA wires, strands, and cables to evaluate their shape memory effects. A full-scale concrete beam was also produced to further verify the proposed concept. Finite-element analysis was performed to simulate the behavior of the beam end subject to both longitudinal and vertical prestressing forces, which resulted from the steel strands and SMA cables. The test and analysis results are discussed as follows:

1. Both heat gun and direct power supply were used to heat the SMAs at an early stage of the research. The heat gun was not effective because it did not provide uniform heating similar to the electrical heating option. A relatively high current up to 40 amps was necessary to heat the SMAs efficiently.
2. All beam tests showed that prestressing could be successfully introduced when the SMAs were activated.
3. The surface condition of the bonded SMAs apparently influenced the resulting prestress in the beam. The ends of the SMAs may be bent or anchored to leverage the recovery stress and maximize the prestressing.

4. The effectiveness of anchors for unbonded SMAs should be carefully selected to achieve desirable prestressing in the beam. Anchor set losses should be minimized when an unbonded system is implemented.
5. Some of the test results showed that the NiTi SMAs lost most of the recovery stress after the heat was removed. It indicates the need for selecting other SMAs, such as NiTiNb, that have a wide thermal hysteresis in real practices.
6. The provided SMA cables in the full-scale beam caused approximately 1.0 MPa compressive stress in the web, indicating that the resulting prestressing force was significant. When properly designed, the SMAs can eliminate concrete cracking due to bursting forces at prestress release.
7. Finite element models can reasonably simulate the structural response of the beam end zone and account for the prestressing along both longitudinal and vertical directions.

5.2 UHPC Girder End Zone

Use of UHPC results in a shorter transfer length as compared to that of conventional concrete. A shorter transfer length indicates that the prestressing force is introduced to the girder end more abruptly, causing larger tensile stresses at the girder end. On the other hand, however, the UHPC's post-cracking tensile strength contributes to the bursting resistance in addition to the reinforcing bars. The resulting bursting force is a function of numerous parameters, including the total prestressing force, layout of top and bottom prestressing strands, girder section properties (e.g., centroid and depth), strand transfer length, etc. The use of post-tensioning strands at the girder flange top resulted in higher

rebar stresses in comparison with pretensioning strands because the prestressing force was transferred to the girder end without involving a strand transfer length.

In accordance with the current AASHTO LRFD Bridge Design Specifications, it is recommended that the bursting force is designed for 4 percent of the prestressing force, which is carried by the reinforcing steel located within a quarter of girder height. Because UHPC has a high post-cracking tensile strength, it should be factored into bursting resistance calculations. The tensile stress limit of the reinforcing bars, 20 ksi, is specified to control the crack width in conventional concrete girders. The collected strain gauge readings in the tested specimens indicate that the resulting bursting stresses in the UHPC were less than this limit and no visible cracks were found.

In UHPC girders, the same tensile stress limit for reinforcing bars can be used conservatively because the crack width is expected to be further reduced due to the existence of steel fibers in UHPC. Researchers proposed different recommendations on UHPC's bursting resistance. Several researchers suggested using 0.75 ksi as the average tensile strength at the end zone. Tadros suggested a conservative stress distribution for UHPC varying from 0 to 0.75 ksi instead.

The finite element analyses showed reasonable agreement with the testing data without being unduly conservative. Reinforcing bar stresses observed were constantly less than the current 20 ksi limit. The bursting force-to-prestressing force ratios were mostly less than 4% and the crack length were still generally limited to within $h/4$ of the length of the girder from the end. However, a shape factor might be applicable to cater for deeper girders, which may be further verified in future studies.

The investigation into the deep girders revealed that an end zone of $h/8$ may be more appropriate. Given that the section is deep, $h/4$ is greater than the transfer length. Hence, $h/4$ may be too large for the layout of the reinforcement bars as observed in the stresses having reduced significantly beyond $h/8$ implying a minimal contribution from those bars. Therefore, placing the steel reinforcement within with $h/8$ of the the end zone where the demand is highest is a better option. Further studies on intermediate girder depth may be necessary to determine the starting point of deep girder behavior.

Furthermore, the stress in the steel reinforcements closest to the end zone exceeded the current 20 ksi limit in all the cases considered for models based on the experimental beams and the deep girders in **Table 4-5**. However, this value was based on crack control in conventional concrete which may not be applicable to UHPC. The findings in **Table 4-7** suggest that by carefully selecting the location and amount of steel of first bar and, the spacing between the bars in the end zone, it was possible for the steel stress to be reasonably close to the 20 ksi limit even with a post-cracking strength of 0.75 ksi. This is important because there are UHPC classes that may not meet 1.5 ksi assumption. However, it is possible that a limit of 36 ksi on steel stress may be more appropriate for UHPC, subject to confirmation from future experimental studies.

In **Figure 5-1** the relationship between the total bursting forces and the total prestressing forces in the experimental and analytical studies is shown. Girder B and the deep girder were the cases considered. For Girder B, additional analyses were carried out for 1.0 ksi and 0.75 ksi UHPC post-cracking tensile strength. Three lines corresponding to various ratios, 2%, 3%, and 4% of splitting forces with respect to the applied prestressing forces due to bottom strands only and total strands were also included. It was

found that the bursting force-to-prestressing force ratios of the girders generally varied from 2% to 4%. Only the model for Girder B with 1.5 ksi post-cracking stress slightly exceeded its corresponding 4% P_{pi} at 4.83%. From our findings, it is still acceptable to estimate the bursting force as 4% P_{pi} for the shallow and deep girders because of the evidence in all the cases considered.

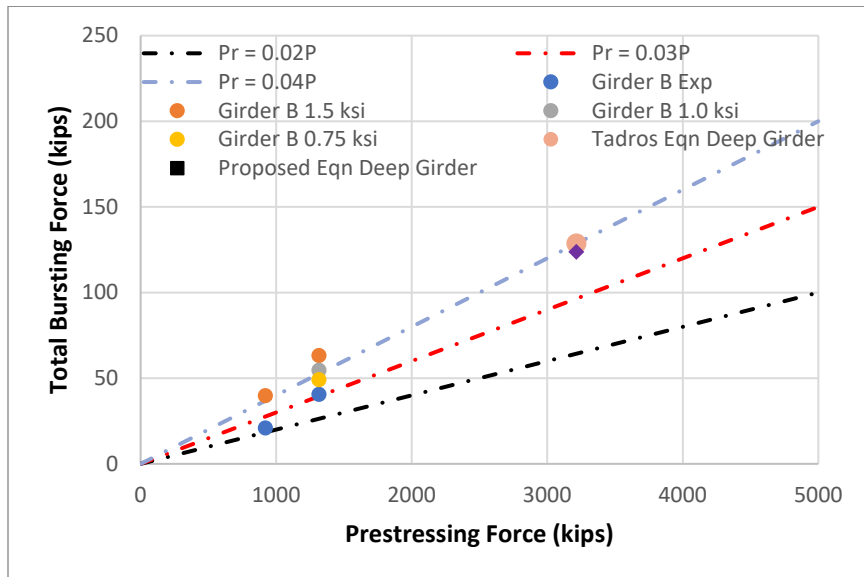


Figure 5-1: ANSYS bursting forces.

CHAPTER 6

CONCLUSIONS

Experimental work was conducted on the use of shape memory alloy (SMA) wire to apply vertical prestress in the end zone of prestressed girders to counter the bursting stresses due to prestress transfer. Another approach was to focus on the end zone behavior of ultra-high performance concrete (UHPC) since this is a relatively newer material that is bound to gain more traction in construction of optimized girders over long spans. The amount of reinforcement in the UHPC girder and prestressing force were the variables for the project and strain data was collected. Based on the lab testing and analysis results, the following conclusions are drawn:

1. The provided SMA cables in the full-scale beam resulted in appreciable compressive stress in the web.
2. The recovery stress of the NiTi cables was mostly lost after the electrical heating was removed. However, the lab testing validated the proposed concept of introducing vertical prestress through SMAs at the concrete beam ends.
3. Other types of SMAs, such as NiTiNb, seem to be more suitable in providing permanent prestressing with their wide thermal hysteresis.
4. When a SMA cable is located within a distance of $h/4$ (h = beam height) from the beam end, its contribution to the splitting resistance appears to be more effective.

5. The use of SMAs can successfully introduce vertical prestress at the prestressed concrete beam ends, and therefore can increase the splitting resistance and avoid concrete cracking at prestress release.
6. When SMA cables are electrically heated to provide the vertical prestress in concrete beams, their anchors should be carefully selected to minimize the anchor set losses and leverage recovery stress.

Based on the limited lab testing and finite element analyses along with the literature review, **Eq. 6-1** is recommended to account for the splitting resistance due to reinforcing steel and UHPC. This equation is based on assumptions that the end zone is either $h/8$ for deeper girders or $h/4$ for shallower sections ($h =$ girder height) and the post-cracking tensile strength of UHPC is 0.75 ksi for an appropriate length. The allowable tensile stress of reinforcing steel is limited to 20 ksi to control the crack width.

$$P_r \leq f_s A_s + 0.75 f_{rr} L_{ez} b_v \quad \text{Eq. 6-1}$$

Where:

f_s = allowable stress in steel. 20 ksi can be tentatively used until future experimental studies can justify a higher stress limit for UHPC girders.

A_s = total area of vertical reinforcement located within a distance of $h/4$ from the girder end.

f_{rr} = post-cracking residual tensile strength = 0.75 ksi unless a higher value can be justified by laboratory tests (e.g., direct tensile test).

L_{ez} = end zone either $h/8$ for deeper girders or $h/4$ for shallower sections

b_v = web width

APPENDIX A

ANSYS COMMAND SNIPPET FOR NODE MERGE AND PRESTRESS SPECIFICATION

ANSYS command snippet for node merge and prestress specification

! Commands inserted into this file will be executed just prior to the ANSYS SOLVE command.

! These commands may supersede command settings set by Workbench.

! Active UNIT system in Workbench when this object was created: U.S. Customary (in, lbf, s, V, A)

! NOTE: Any data that requires units (such as mass) is assumed to be in the consistent solver unit system.

! See Solving Units in the help system for more information.

```
/PREP7
```

```
CMSEL,S,Concrete,ELEM  
!CMSEL,A,Strands,ELEM  
CMSEL,A,Rebars,ELEM  
NSLE,S,ALL
```

```
INUMMRG, Label, TOLER, GTOLER, Action, Switch  
NUMMRG, NODES, .1, , ,
```

```
ALLSEL,ALL
```

```
CMSEL,S,Concrete,ELEM  
CMSEL,A,Strands,ELEM  
!CMSEL,A,Rebars,ELEM  
NSLE,S,ALL
```

```
INUMMRG, Label, TOLER, GTOLER, Action, Switch  
NUMMRG, NODES, .1, , ,
```

```
ALLSEL,ALL
```

```
!!Assign Element to Concrete
!*SET,ELEM_TYPE_ID,1001
!CMSEL,S,Concrete,ELEM
!EMODIF,ALL,TYPE,ELEM_TYPE_ID

!*SET,ELEM_TYPE_ID,1001
!EMODIF,ALL,MAT,ELEM_TYPE_ID
!!*SET,MATID,ELEM_TYPE_ID
!ALLSEL,ALL

!Assign Element to Rebars
*SET,ELEM_TYPE_ID,1002
CMSEL,S,Rebars,ELEM
EMODIF,ALL,TYPE,ELEM_TYPE_ID
ALLSEL,ALL

CMSEL,S,Rebars,ELEM
EMODIF,ALL,MAT,ELEM_TYPE_ID
ALLSEL,ALL

!Assign Section
CMSEL,S,Rebars,ELEM
EMODIF,ALL,SECNUM,ELEM_TYPE_ID
ALLSEL,ALL

!Assign Element to Strands
*SET,ELEM_TYPE_ID,1003
CMSEL,S,Strands,ELEM
EMODIF,ALL,TYPE,ELEM_TYPE_ID
ALLSEL,ALL

*SET,ELEM_TYPE_ID,1003
CMSEL,S,Strands,ELEM
EMODIF,ALL,MAT,ELEM_TYPE_ID
ALLSEL,ALL

!Assign Section
*SET,ELEM_TYPE_ID,1003
CMSEL,S,Strands,ELEM
EMODIF,ALL,SECNUM,ELEM_TYPE_ID
ALLSEL,ALL

fini

/SOLU
```

```
CMSEL,S,Pretensioned,ELEM
INISTATE, SET, DTYP, STRE, , , , , ,
INISTATE, SET, MAT,ELEM_TYPE_ID,0!
INISTATE, DEFINE,,,,,202300,,,, !To apply 43.9 kips
!INISTATE, DEFINE,,,,,182070,,,, !To apply 90% of P
!INISTATE, DEFINE,,,,,101150,,,, !To apply 50%
ALLSEL,ALL
```

```
NEQIT,500
```

```
OUTRES,ALL,ALL
```

REFERENCES

- Alam, M. S., Youssef, M. A., & Nehdi, M. (2007). Utilizing shape memory alloys to enhance the performance and safety of civil infrastructure: A review. *Canadian Journal of Civil Engineering*, 34(9), 1075–1086. <https://doi.org/10.1139/L07-038>
- American Association of State Highway and Transportation Officials. (2020). *AASHTO LRFD Bridge Design Specifications, 9th Edition*. AASHTO LRFD Bridge Design Specifications, 1661.
- Andrawes, B. (2019). Adaptive Prestressing System for Concrete Crossties. (No. Rail Safety IDEA Project 33). <https://trid.trb.org/view/1688130>
- Behloul, M. (2000). Design rules for DUCTAL pre stressed beams. Technical Information from Bouygues , 1–15. <https://ci.nii.ac.jp/naid/10010174029/>
- Castrodale, R., Lui, A., & White, C. D. (2002). Simplified Analysis of Web Splitting in Pretensioned Concrete Girders. Proceedings, PCI/FHWA/NCBC Concrete Bridge Conference, Nashville, TN.
- Chen, L., & Graybeal, B. A. (2012). Modeling Structural Performance of Ultrahigh Performance Concrete I-Girders. *Journal of Bridge Engineering*, 17(5), 754–764. [https://doi.org/10.1061/\(ASCE\)be.1943-5592.0000305](https://doi.org/10.1061/(ASCE)be.1943-5592.0000305)
- Cousins, T. E., Roberts-Wollmann, C. L., Crispino, E. D., & Roberts, C. L. (2009). Anchorage zone design for pretensioned precast bulb-T bridge girders in Virginia. Virginia Center for Transportation Innovation and Research. <https://vtechworks.lib.vt.edu/handle/10919/46639>
- Davis, R. T., Buckner, D. C., & Ozyildirim, C. (2005, October). Serviceability-based design method for vertical beam end reinforcement. Proceedings, PCI National Bridge Conference.
- Devalapura, R., Journal, M. T.-P., & 1992, undefined. (1992). Stress-strain modeling of 270 ksi low-relaxation prestressing strands. *PCI Journal*, 37(2), 100–106.
- El-Tawil, S., & Ortega-Rosales, J. (2004). Prestressing concrete using shape memory alloy tendons. *Structural Journal*, 101(6), 846–851. <https://www.concrete.org/publications/internationalconcreteabstractsportal/m/details/id/13460>

- Gergely, P., & Sozen, M. A. (1967). Design of Anchorage-Zone Reinforcement in Prestressed Concrete Beams. *PCI Journal*, 12(2), 63–75.
<https://doi.org/10.15554/pcij.04011967.63.75>
- Gowripalan, N., & Gilbert, R. I. (2000). Design guidelines for ductal prestressed concrete beams. Design guide . Civil & Environmental Engineering School, University of NSW, Sydney, Australia.
- Hamilton, H. R., Consolazio, G. R., & Torres, E. (2020). Hybrid Prestressed Concrete Bridge Girders Using Ultra-High Performance Concrete.
- Kannel, J. J., French, C. E., Stolarski, H. K., University of Minnesota, T. C., & Minnesota Department of, T. (1998). Release Methodology of Prestressing Strands. 257 p. <https://trid.trb.org/view/654667>
- Lenschow, R. o l f J. ., & Sozen, M. A. (1965). Practical analysis of the anchorage zone problem in prestressed beams. *ACI Journal Proceedings*, 62(11), 1421–1440.
<https://www.concrete.org/publications/internationalconcreteabstractsportal/m/details/id/7754>
- Maji, A. K., & Negret, I. (1998). Smart Prestressing with Shape-Memory Alloy. *Journal of Engineering Mechanics*, 124(10), 1121–1128. [https://doi.org/10.1061/\(ASCE\)0733-9399\(1998\)124:10\(1121\)](https://doi.org/10.1061/(ASCE)0733-9399(1998)124:10(1121))
- Marshall, W. T., & Mattock, A. H. (1962). Control of Horizontal Cracking in the Ends of Pretensioned Prestressed Concrete Girders. *PCI Journal*, 7(5), 56–74.
<https://doi.org/10.15554/pcij.10011962.56.74>
- Mohebbi, A., El-Helou, R., & Graybeal, B. (2019). End Zone Design and Behavior of Prestressed UHPC Girders. 2019 International Accelerated Bridge Construction Conference, Including Automation, Service Life and Ultra High-Performance Concrete, 287–289.
- Moser, K., Bergamini, A., Christen, R., & Czaderski, C. (2005). Feasibility of concrete prestressed by shape memory alloy short fibers. *Materials and Structures*, 38(5), 593–600. <https://doi.org/10.1007/BF02479551>
- Okumus, P., & Oliva, M. G. (2013). Evaluation of crack control methods for end zone cracking in prestressed concrete bridge girders. *PCI Journal*, 58(2), 91–105.
<https://doi.org/10.15554/PCIJ.03012013.91.105>
- Ozbulut, O., & Hamilton, R. (2015). Smart Concrete Bridge Girders Using Shape Memory Alloys. <https://trid.trb.org/view/1424165>
- Rogowsky, D. M., & Marti, P. (1991). Detailing for Post-Tensioned. VSL Report Series, 3.

- Ronanki, V. S., Aaleti, S., & Binard, J. P. (2019). Long-Span Hybrid Precast Concrete Bridge Girder Using Ultra-High-Performance Concrete and Normalweight Concrete. *PCI Journal*, 64(6). <https://doi.org/10.15554/pcij64.6-02>
- Russell, H., Graybeal, B., & Russell, H. (2013). Ultra-high performance concrete: a state-of-the-art report for the bridge community. <https://rosap.nrl.bts.gov/view/dot/26387>
- Sherif, M., Ozbulut, O., Landa, A., & Hamilton, R. F. (2014). Self-post-tensioning for concrete beams using shape memory alloys. *Proceedings of the ASME Smart Materials, Adaptive Structures and Intelligent Systems*, 46155. <https://asmedigitalcollection.asme.org/SMASIS/proceedings-abstract/SMASIS2014/V002T04A014/286169>
- Sinha, A., Tatar, N., & Tatar, J. (2020). Rapid heat-activated post-tensioning of damaged reinforced concrete girders with unbonded near-surface mounted (NSM) NiTiNb shape-memory alloy wires. *Materials and Structures/Materiaux et Constructions*, 53(4). <https://doi.org/10.1617/S11527-020-01522-8>
- Soroushian, P., Ostowari, K., Nossoni, A., & Chowdhury, H. (2001). Repair and strengthening of concrete structures through application of corrective posttensioning forces with shape memory alloys. *Transportation Research Record*, 1770, 20–26. <https://doi.org/10.3141/1770-03>
- Tadros, M. K., Badie, S. S., & Tuan, C. Y. (2010). *Evaluation and Repair Procedures for Precast/Prestressed Concrete Girders with Longitudinal Cracking in the Web*. National Academies Press. <https://doi.org/10.17226/14380>
- Tadros, M., Lawler, J., El-Khier, M., Gee, D., Kurt, A., Lucier, G., & Wagner, E. (2021). *Implementation of Ultra-High Performance Concrete in Long-Span Precast Pretensioned Elements for Concrete Buildings and Bridges*.
- Tuan, C. Y., Yehia, S. A., Jongpitaksseel, N., Tadros, M. K., Tuan, C. Y. ;, Yehia, S. A. ;, & Jongpitaksseel, N. ; (2004). *End Zone Reinforcement for Pretensioned Concrete Girders Recommended Citation*. <https://digitalcommons.unomaha.edu/civilengfacpub/1>